Computer Modeling in Engineering & Sciences

Tech Science Press

https://doi.org/10.32604/cmes.2026.087072

ARTICLE

Dynamical Analysis of the Fractional-Order Chialvo Neuron Map: Synchronization, Multistability, and Extreme Events

Anitha Karthikeyan[1], **Mahtab Mehrabbeik**[2], **Karthikeyan Rajagopal**[3,4], **Sajad Jafari**[2,5] and **Matjaž Perc**[6,7,8,9,*]

[1]Center for Cognitive Science, Trichy SRM Medical College Hospital and Research Center, Trichy, India
[2]Department of Biomedical Engineering, Amirkabir University of Technology (Tehran Polytechnic), Tehran, Iran
[3]Center for Research, Easwari Engineering College, Chennai, India
[4]Center for Research, SRM TRP Engineering College, Trichy, India
[5]Health Technology Research Institute, Amirkabir University of Technology (Tehran Polytechnic), Tehran, Iran
[6]Faculty of Natural Sciences and Mathematics, University of Maribor, Maribor, Slovenia
[7]Community Healthcare Center Dr. Adolf Drolc Maribor, Maribor, Slovenia
[8]University College, Korea University, Seoul, Republic of Korea
[9]Department of Physics, Kyung Hee University, Seoul, Republic of Korea

*Corresponding Author: Matjaž Perc. Email: matjaz.perc@gmail.com

Received: 10 June 2026; Accepted: 08 September 2026; Published: 21 October 2026

ABSTRACT: A two-dimensional fractional-order Chialvo neuron map based on the Caputo fractional difference operator is studied, extending the classical discrete model by incorporating memory effects while retaining the computational simplicity and efficiency of map-based neurons. Stability analysis shows that the map possesses a unique equilibrium with a complex-conjugate pair of eigenvalues, which is asymptotically stable below a critical fractional order and loses stability above it through a Neimark–Sacker bifurcation. Strong memory thus stabilizes the resting state, whereas weak memory initiates the transition to oscillatory and ultimately chaotic firing. Bifurcation and Lyapunov analyses reveal that reducing the fractional order displaces the regime sequence toward lower parameter values, enlarges the fixed-point region, and weakens the chaos. Synchronization is then examined for 100 globally coupled maps under electrical, inner-linking, and chemical couplings. Complete synchronization is attained under all three schemes, preceded by antiphase cluster synchronization and solitary states under the diffusive couplings, whereas chemical coupling additionally produces synchronized oscillation death, phase synchronization, and a period-doubling route on the synchronization manifold. Although no coexisting attractors are found for the isolated neuron, the diffusively coupled network supports several distinct dynamical states simultaneously. Extreme events emerge only at the onset of desynchronization, identifying the coupling strength as their controlling parameter. These findings indicate that the fractional-order Chialvo map captures rich memory-dependent neuronal dynamics and provides a useful model for studying multistability, rare events, and synchronization phenomena in computational neuroscience.

KEYWORDS: Fractional-order; Chialvo map; multistability; extreme event; synchronization

1 Introduction

Mathematical neuronal models facilitate extensive research on brain neuronal activity, as they directly help elucidate its underlying mechanisms [1–3]. These neuronal models can be defined as continuous-time and discrete-time systems, also known as flow-based and map-based models [4]. The Hodgkin-Huxley (HH) [5] and Hindmarsh-Rose (HR) [6] neuron models are prominent examples of flow-based neuronal

Copyright © 2026 The Authors. Published by Tech Science Press. This work is licensed under a Creative Commons Attribution 4.0 International License, which permits unrestricted use, distribution, and reproduction in any medium, provided the original work is properly cited.

models described by differential equations. Similarly, the Rulkov [7] and the Chialvo [8] maps are well-known discrete-time systems defined by difference equations. Map-based models are more efficient than flow-based ones in terms of computational cost and execution time. Furthermore, they are more flexible and straightforward in definition [4]. Memory in map-based neuron models is diverse, arising from dynamic behaviors and attractors. It includes sensitivity to initial conditions, bifurcation memory, transient memory, hysteresis, and stochastic elements. These models effectively store and recall information through various mechanisms, contributing to their rich memory characteristics [4]. In computational neuroscience, discrete models are crucial for representing neuron and neuronal network dynamics, especially for computational efficiency. Neuronal processes, like action potentials and synaptic events, are inherently discrete and chaotic [9], making discrete modeling highly appropriate [10]. These models can efficiently track individual spikes in large networks, describe synaptic plasticity, and simulate collective network behavior [4]. By aligning with the inherent discreteness of neural processes, discrete modeling helps understand brain computations across different scales. Therefore, map-based models, especially in neuronal studies, have recently gained attention. A considerable number of studies have proposed new map-based neuron models. For example, applying the forward Euler method, Li and He [11] proposed the two-dimensional HR neuron map. Using a similar discretizing method and adding a discrete memristor, Bao et al. [12] introduced the memristive version of the HR neuron maps. Zandi-Mehran et al. [13] showed how a piecewise nonlinear one-dimensional map could mimic the behavior of a biological neuron model. Thereafter, the memristive version of the neuron proposed by Zandi et al. was presented by Ramakrishnan et al. [14]. Similarly, Li et al. [15] introduced the memristive Rulkov neuron map by adding a discrete memristor.

While the origins of fractional calculus date back centuries to the time of Leibniz, the subfield of discrete fractional calculus, which deals with fractional-order differences and sums of discrete functions, is a more recent development, emerging over the past 40 years [16]. Diaz and Osler [17] introduced discrete fractional difference operators in 1974, followed by more robust definitions by Gray and Zhang [18] in 1988, which provided a rigorous mathematical framework. Since then, discrete fractional calculus has rapidly expanded, with various generalizations of the discrete fractional operators and growing research into numerical methods and diverse applications ranging from mathematical physics to biological modeling [19]. Currently, the characterization of fractional-order discrete systems predominantly relies on three principal definitions: the Riemann–Liouville, Caputo, and Grünwald–Letnikov definitions [20]. Within this context, the Riemann–Liouville definition requires the specification of initial conditions, while research on the Grunwald–Letnikov definition is comparatively limited, with several of its features lacking in-depth analysis. The Caputo fractional difference operator is a discrete analog of the Caputo fractional derivative and offers a versatile, practical tool for modeling and analyzing systems with fractional-order dynamics [21,22]. Its advantages include consistency with initial conditions, numerical stability, applicability across various fields, and the ability to describe complex real-world phenomena [23,24] accurately. In other words, the Caputo definition not only sidesteps the issue of initial value definition but also benefits from extensive theoretical research and comprehensive analysis.

In mathematical analysis, fractional calculus is a rapidly growing field that examines the influence of a model's history on its current dynamics. In other words, it involves the effect of memory [25–27]. Therefore, in real-world applications, fractional calculus can help model memory-dependent processes, such as neuronal ones, more accurately [28–30]. Fractional calculus enables the development of neuron models that can effectively represent intricate spatiotemporal patterns, memory effects, and complicated interactions in biological neuronal systems [31]. This versatility makes fractional modeling a valuable tool for understanding how neurons compute and how the brain's physiology works. The inherent non-locality and historical dependence of fractional systems align with the integrative nature of neural circuits, enhancing

their suitability for modeling neural processes [32]. Generally, lower fractional orders are associated with modeling faster, more localized neural activity, while higher orders are associated with describing slower, non-local, and memory-dependent neural behaviors [33]. Hence, several fractional-order (FO) neuronal models, both flow-based and map-based, have been proposed in the literature. For instance, Jun et al. [31] studied the firing behaviors of the FO HR neurons. According to their declarations, the FO HR model more closely mimics actual neuronal firing activity. Yu et al. [34] introduced the FO memristive HR neuron model and studied its hidden dynamics. In another study conducted by Chen et al. [35], the FO HH neuron model was introduced, and the influence of the fractional order on the Hopf bifurcation was examined. They also developed a control method. Lu et al. [20] studied the dynamics of the Rulkov neuron map with a fractional-order discrete memristor. In another study by Alkhalaf et al. [36], a one-dimensional FO Rulkov map was presented and its dynamics investigated. They announced that FO Rulkov neurons could exhibit chaotic behavior without time-dependent input. Similarly, Vivekanandhan et al. [37] conducted a study on the different dynamics of two-dimensional Rulkov maps. Teka et al. [38] investigated the firing patterns of the FO Izhikevich neuron model that emerged as a result of employing fractional calculus. The FO memristive modified Nagumo-Sato neuron map was proposed by Ramadoss et al. [39]. They also performed a dynamical analysis and studied the network behavior of the proposed FO map.

Multistability is a widespread dynamical behavior, observed in both physical and biological systems [40,41]. It refers to the coexistence of several stable solutions for a fixed parameter setting, the particular solution reached being determined by the choice of initial condition. Extreme multistability and megastability are two special cases in which infinitely many attractors coexist; in the former, the attractors are uncountable, whereas in the latter they are countable [42,43]. Multistability may arise in the dynamics of an isolated model [43,44] or emerge from interactions among network units [45,46].

Extreme events are another important dynamical behavior, characterized by intense fluctuations in the system's behavior. Such events are almost unwanted and unpredictable; thus, the study of extreme events has become a challenging issue among researchers [47,48]. Mishra et al. [49] observed the occurrence of extreme events in two HR neurons coupled via chemical synapses and a diffusive coupling function. Besides, Ray et al. [50] reported the appearance of extreme events in the behavior of the Ikeda map. Similarly, extreme events were observed for two electrically coupled FitzHugh-Nagumo neurons by Ansmann et al. [51].

Aside from investigating the dynamics of isolated neuron models, the study of neuronal dynamics arising from interactions among interconnecting neurons is another attractive field of research. In this field of study, synchronization is considered the most important collective dynamic underlying many biological processes [52,53]. Synchronization is a general concept consisting of different branches, such as complete synchronization [54], phase synchronization [55], and partial synchronization [56]. For instance, phase synchronization plays a vital role in human memory processes [53]. Given the importance of synchronization, many studies have investigated the synchronization of neuronal models. For instance, the synchronization of the HR [57,58], Morris-Lecar [59,60], FitzHugh-Nagumo [61,62], and Rulkov [63–65] neurons has been explored in different studies.

In the present paper, the FO Chialvo neuron map is proposed using the Caputo difference operator, and its dynamical properties are investigated via bifurcation and the largest Lyapunov exponent (LLE) diagrams. In this regard, the effects of variations in the fractional-order and model parameters are explored. Furthermore, the synchronization of 100 globally coupled FO Chialvo neuron maps is examined under electrical, inner-linking, and chemical coupling functions. Accordingly, the FO Chialvo map is presented in detail in Section 2. The results of the analyses are presented in Section 3, and Section 4 summarizes the key findings as the conclusion.

2 The Model

2.1 The Chialvo Neuron Model

The Chialvo map is a discrete model of an excitable neuron proposed by Chialvo [8] in 1995. This model describes the generic dynamics of a neuron as a two-dimensional system, defined as

$$\begin{aligned} x(n+1) &= x^2(n)e^{y(n)-x(n)} + k, \\ y(n+1) &= ay(n) - bx(n) + c, \end{aligned} \tag{1}$$

where x and y are the activation/potential and recovery-like variables, furthermore, n is the iteration step showing the discrete time evolution of the model, k is the bias or additive perturbation, a ($a < 1$) is a constant denoting the recovery time, b ($b < 1$) is a parameter representing the dependence of the recovery state on the activation process, and, eventually, c is the offset. Depending on parameter settings, the Chialvo neuron model can exhibit various firing modes, including periodic and chaotic firing.

Fig. 1 demonstrates the chaotic bursting activity of the Chialvo neuron through its phase diagram and the time series for the fixed parameters $a = 0.89$, $b = 0.18$, $c = 0.28$, and $k = 0.03$. The phase portrait in Fig. 1a combines a dense inner spiral, corresponding to small-amplitude subthreshold oscillations, with large excursions representing the spiking phase, and the time series in Fig. 1b shows the resulting alternation between low-amplitude activity and irregular high-amplitude spikes that characterizes chaotic bursting. The map is iterated from the initial condition $(x(0), y(0)) = (1, 1)$, which is retained for all simulations of the isolated neuron.

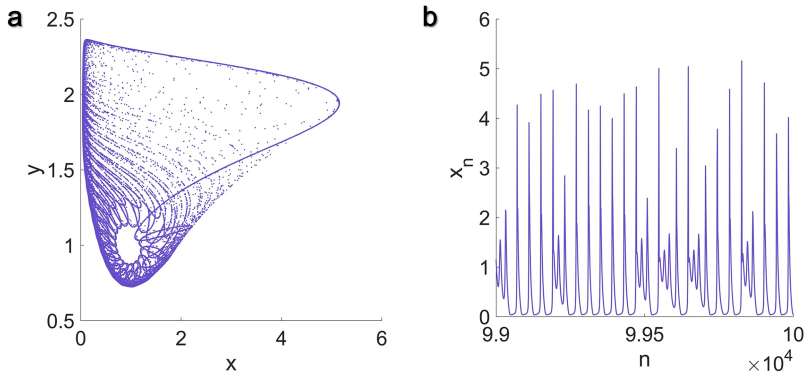


Figure 1: (**a**) The phase diagram and (**b**) time series of the two-dimensional Chialvo neuron map for $a = 0.89$, $c = 0.28$, $b = 0.18$, and $k = 0.03$, obtained from the initial condition $(x(0), y(0)) = (1, 1)$. The trajectory fills a broad region of the phase plane, and the spike amplitudes vary irregularly from one event to the next, confirming chaotic firing in this parameter regime.

The dynamical richness of the Chialvo map is investigated through bifurcation and Lyapunov analysis in Figs. 2 and 3. Fig. 2a,c,d shows the dynamical behavior of the Chialvo neuron for $a \in [0.875, 0.915]$ (with $b = 0.18$, $c = 0.28$, and $k = 0.03$), $c \in [0.25, 0.3]$ ($a = 0.89$, $b = 0.18$, and $k = 0.03$), and $k \in [0.0195, 0.074]$ (with $a = 0.89$, $b = 0.18$, and $c = 0.28$), respectively, all of which share the same behavioral structure. In these settings, no spiking activity is detected at either end of the intervals, where the dynamics settle onto stable fixed points. As the bifurcation parameter increases, the neuron abruptly enters chaotic bursting through a boundary crisis, and the burst amplitude then grows monotonically over a broad band of parameter values. Within this band, many periodic windows are recognized, which repeatedly interrupt the chaotic dynamics. Beyond this band, the range of chaotic spike amplitudes contracts smoothly over a narrow interval, after

which the dynamics pass through a periodic stage into quasiperiodic motion. Although the ranges of the studied parameters are not identical, quasiperiodic dynamics are more prominent under variation of k, whereas the most extensive chaotic behavior appears under variation of c.

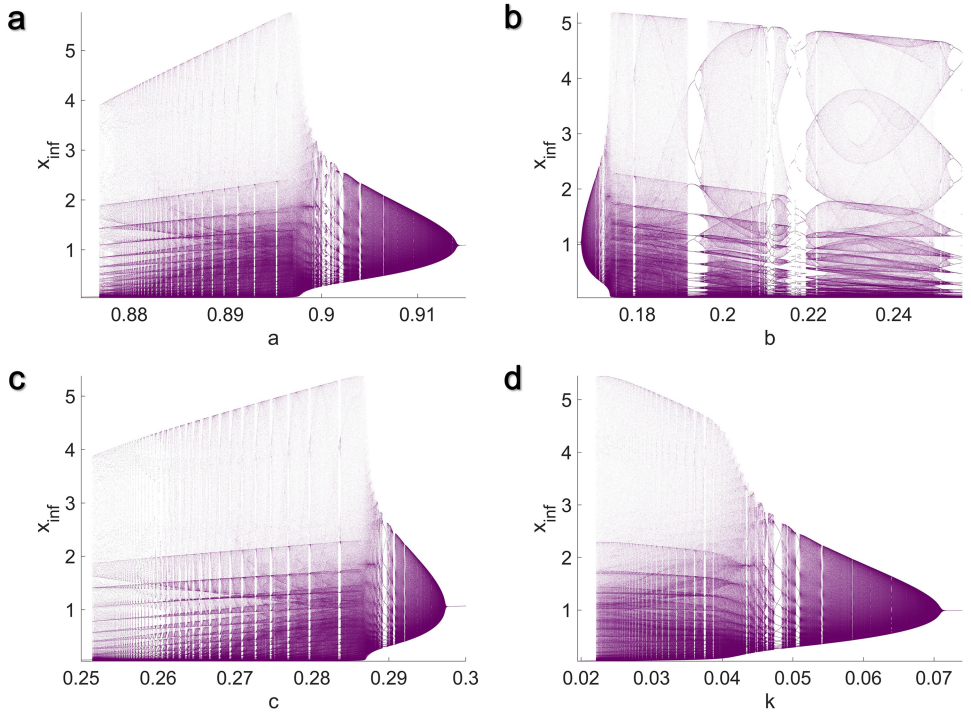


Figure 2: The bifurcation diagrams of the Chialvo neuron map as a function of (**a**) parameter a ($a \in [0.875,\ 0.915]$, $b = 0.18$, $c = 0.28$, and $k = 0.03$), (**b**) parameter b ($b \in [0.166,\ 0.256]$, $a = 0.89$, $c = 0.28$, and $k = 0.03$), (**c**) parameter c ($c \in [0.25,\ 0.3]$, $a = 0.89$, $b = 0.18$, and $k = 0.03$), and (**d**) parameter k ($k \in [0.0195,\ 0.074]$, $a = 0.89$, $b = 0.18$, and $c = 0.28$), obtained from the initial condition $(x(0), y(0)) = (1, 1)$. The vertical axis shows the asymptotic values x_{inf} of the activation variable after the transient has been discarded. Panels (**a**,**c**,**d**) follow the same route—fixed point, chaotic bursting, quasiperiodic motion, fixed point—whereas in panel (**b**) the ordering is reversed, with the map entering chaos as b increases and remaining chaotic to the end of the interval.

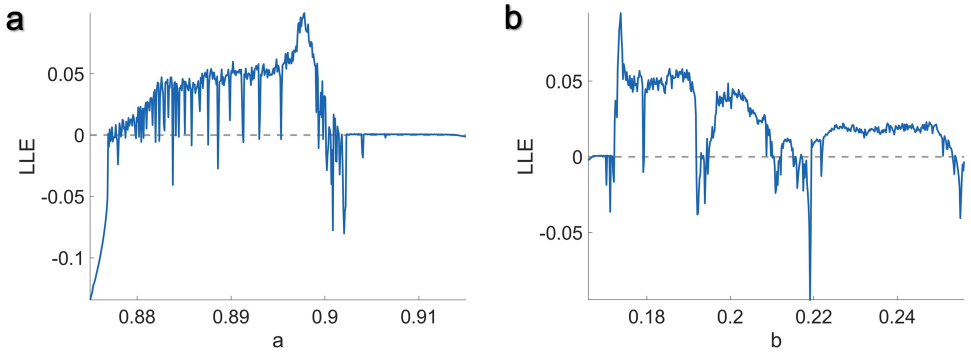


Figure 3: (Continued)

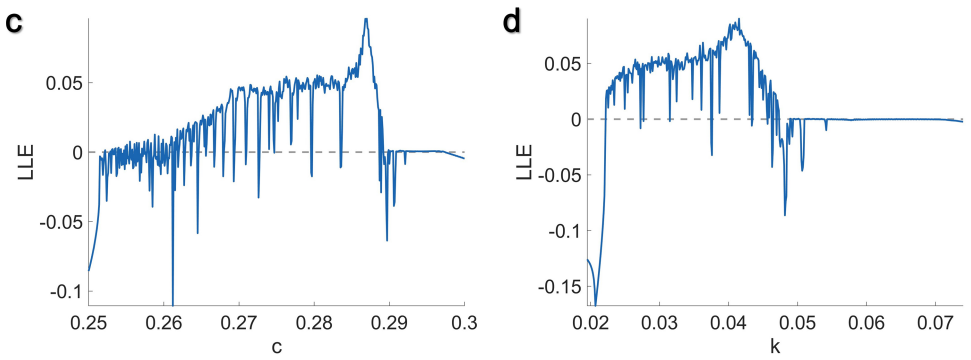


Figure 3: The LLE diagrams of the Chialvo neuron map as a function of (**a**) parameter a ($a \in [0.875,\ 0.915]$, $b = 0.18$, $c = 0.28$, and $k = 0.03$), (**b**) parameter b ($b \in [0.166,\ 0.256]$, $a = 0.89$, $c = 0.28$, and $k = 0.03$), (**c**) parameter c ($c \in [0.25,\ 0.3]$, $a = 0.89$, $b = 0.18$, and $k = 0.03$), and (**d**) parameter k ($k \in [0.0195,\ 0.074]$, $a = 0.89$, $b = 0.18$, and $c = 0.28$), computed over the same parameter scans as Fig. 2 from the initial condition $(x(0), y(0)) = (1, 1)$. The dashed line marks $LLE = 0$. Positive values identify the chaotic bands of Fig. 2, negative values correspond to the fixed-point regions and the periodic windows, and zero values indicate the quasiperiodic regions.

On the other hand, the behavior obtained by varying $b \in [0.166, 0.256]$ (with $a = 0.89$, $c = 0.28$, and $k = 0.03$), shown in Fig. 2b, follows a different order: fixed-point dynamics occupy only the beginning of the interval, and the map then remains chaotic up to its end. Within the chaotic region, significant periodic windows are identified. The first considerable one, at $b \approx 0.1916$, is entered from chaos through a boundary crisis and left through a period-doubling route back into chaos. Moreover, once the chaotic region is re-entered, the amplitude of the chaotic attractor increases abruptly via an interior crisis. The second periodic window is entered through an inverse period-doubling cascade and left through a period-doubling route. At the end of the interval, the large-amplitude component of the attractor disappears through a further interior crisis. Then, through an inverse period-doubling route, the chaotic dynamics are replaced by periodic motion, forming a further periodic window. Only the onset of this window falls within the studied interval.

These dynamics are verified through the LLE diagrams in Fig. 3, which correspond to the same parameter scans as the panels of Fig. 2. Fig. 3 shows positive values in the chaotic regions, negative values at the fixed points and within the periodic windows, and zero values in the quasiperiodic regions identified in the bifurcation diagrams; the sharp downward spikes of the LLE coincide with the periodic windows visible in Fig. 2. According to Fig. 3a,c,d, the LLE increases over most of the chaotic band as the control parameter grows, reaching its maximum shortly before the transition out of chaos, while in Fig. 3b the LLE attains its maximum at the beginning of the chaotic region and decreases as b increases. Overall, the maximum LLE reached in the chaotic regions is of the order of 0.05 in all panels.

2.2 The FO Chialvo Neuron Model

The main objective of this paper is to investigate the dynamics of the FO Chialvo map by reformulating System (1) using Caputo's left fractional difference [28]. The integer-order map is Markovian, so the adaptation and correlations it produces decay exponentially with a single timescale. Neuronal dynamics are not of this kind: cortical pyramidal neurons perform fractional-order differentiation of their input, adapting according to a power law over several decades of time [66], and the membrane behaves as a non-ideal capacitor whose fractional impedance alters spiking in conductance-based models [33]. Reproducing such behavior in an integer-order framework requires many auxiliary variables spanning a range of time constants,

whereas the Caputo difference achieves it through the single parameter q, which sets the decay exponent of the memory kernel and recovers the memoryless map at $q = 1$.

Letting Δ_{α}^{q} be the symbol of Caputo's left fractional operator and $N_{\alpha} = \{\alpha, \alpha+1, \alpha+2, \ldots\}$, for $q > 0$ ($q \notin N$), the q^{th} order Caputo-like discrete fractional difference can be defined as [21,28]

$$\Delta_{\alpha}^{q} u(\tau) = \Delta_{\alpha}^{-(m-q)} \Delta^{m} u(\tau) = \frac{1}{\Gamma(m-q)} \sum_{s=\alpha}^{\tau-(m-q)} (\tau - s - 1)^{(m-q-1)} \Delta^{m} u(s), \tag{2}$$

where α is the initial point of the function $u : N_{\alpha} \to R$, $\tau \in N_{\alpha+m-q}$ and $m = \lceil q \rceil + 1$. Moreover, Δ^{m} is the m-th order forward difference operator defined as

$$\Delta^{m} u(s) = \sum_{k=0}^{m} \binom{m}{k} (-1)^{m-k} u(s+k), \tag{3}$$

and Δ_{α}^{-q} is the q-th fractional sum of u. For $\tau \in N_{\alpha+q}$, Δ_{α}^{-q} is obtained through

$$\Delta_{\alpha}^{-q} u(\tau) = \frac{1}{\Gamma(q)} \sum_{s=\alpha}^{\tau-q} (\tau - s - 1)^{(q-1)} u(s). \tag{4}$$

In Eq. (4), $\tau^{(q)}$ is the falling factorial obeying the following relation

$$\tau^{(q)} = \frac{\Gamma(\tau+1)}{\Gamma(\tau-q+1)} = \tau(\tau-1)\ldots(\tau-q+1). \tag{5}$$

In fact, a function defined on N_{α} (u for $\tau = \alpha \ mod(1)$) can be mapped to the one defined on $N_{\alpha+q}$ ($\Delta_{\alpha}^{-q} u$ for $\tau = (\alpha+q) \ mod(1)$) through the operator Δ_{α}^{-q}. Considering $0 < q < 1$ and $m = 1$, Eq. (2) turns into

$$\Delta_{\alpha}^{q} u(\tau) = \frac{1}{\Gamma(1-q)} \sum_{s=\alpha}^{\tau-(1-q)} (\tau - s - 1)^{(-q)} \Delta u(s). \tag{6}$$

Setting $\alpha = 0$, and considering F as a real-valued function and initial condition of $u(0)$, for $\tau \in N_{1-q}$ Eq. (6) can be rewritten as

$$\Delta_{0}^{q} u(\tau) = F\left(\tau + q - 1, u(\tau + q - 1)\right). \tag{7}$$

Thereafter, the solution of Eq. (7) is given by

$$u(\tau) = u(0) + \frac{1}{\Gamma(q)} \sum_{s=1-q}^{\tau-q} (\tau - s - 1)^{(q-1)} F\left(u(s+q-1)\right). \tag{8}$$

Substituting $s+q$ with i, a numerically more straightforward form of $(\tau - s - 1)^{(q-1)}$ can be considered as

$$(\tau - s - 1)^{(q-1)} = \frac{\Gamma(\tau - s)}{\Gamma(\tau - s - q)} = \frac{\Gamma(\tau - 1 + q)}{\Gamma(\tau - s - q + 1)} = \frac{\Gamma(\tau - i + q)}{\Gamma(\tau - i + 1)}. \tag{9}$$

Thus, Eq. (8) can be reformulated in terms of n, the number of iterations, as follows

$$u(n) = u(0) + \frac{1}{\Gamma(q)} \sum_{l=1}^{n} \frac{\Gamma(n - l + q)}{\Gamma(n - l + 1)} F\left(u(l-1)\right). \tag{10}$$

The Chialvo map described in Eq. (1) can be converted to the classical integer-order difference equation as

$$\Delta x(n) = x^2(n)\, e^{y(n)-x(n)} + k - x(n),$$
$$\Delta y(n) = ay(n) - bx(n) + c - y(n). \tag{11}$$

Employing Eq. (7), the FO Chialvo neuron map can be described as

$$\Delta_\alpha^q x(\tau) = x^2(\tau+q-1)\, e^{y(\tau+q-1)-x(\tau+q-1)} + k - x(\tau+q-1),$$
$$\Delta_\alpha^q y(\tau) = ay(\tau+q-1) - bx(\tau+q-1) + c - y(\tau+q-1), \tag{12}$$

which can be numerically solved according to Eq. (10) [28]

$$x(n) = x(0) + \frac{1}{\Gamma(q)} \sum_{l=1}^{n} \frac{\Gamma(n-l+q)}{\Gamma(n-l+1)} \left(x^2(l-1)e^{y(l-1)-x(l-1)} + k - x(l-1)\right),$$
$$y(n) = y(0) + \frac{1}{\Gamma(q)} \sum_{l=1}^{n} \frac{\Gamma(n-l+q)}{\Gamma(n-l+1)} \left(ay(l-1) - bx(l-1) + c - y(l-1)\right). \tag{13}$$

In practice, for higher values of n, the following equation can be employed to solve the aforementioned solution [37].

$$\frac{\Gamma(n-l+q)}{\Gamma(n-l+1)} = e^{(\ln(\Gamma(n-l+q)) - \ln(\Gamma(n-l+1)))}. \tag{14}$$

Setting $a = 0.89$, $b = 0.18$, $c = 0.28$, and $k = 0.03$, as in Fig. 1, Fig. 4 shows how the fractional order q changes the dynamics of the neuron. More specifically, Fig. 4 indicates that neurons can exhibit quasiperiodic (Fig. 4a), periodic (Fig. 4b), chaotic spiking (Fig. 4c), and chaotic bursting (Fig. 4d) behavior for $q = 0.96$, 0.975, 0.98, and 0.99, respectively.

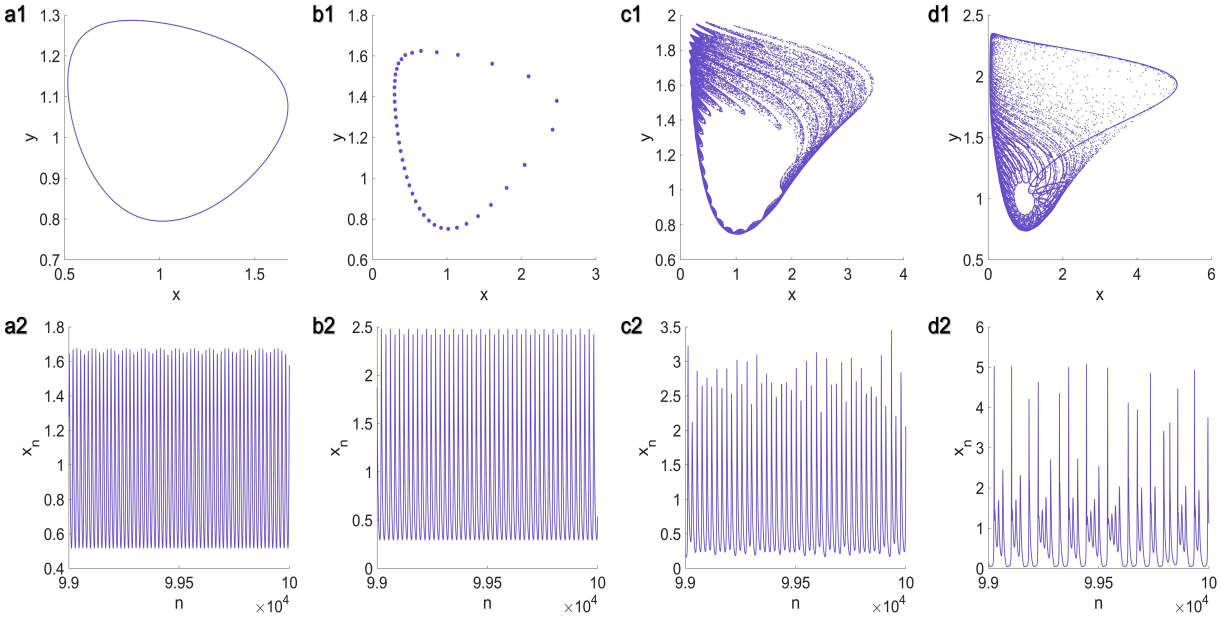


Figure 4: (**a1**–**d1**) The phase diagram and (**a2**–**d2**) time series of the two-dimensional FO Chialvo neuron map for $a = 0.89$, $b = 0.18$, $c = 0.28$, and $k = 0.03$, for different values of fractional order: (**a1**,**a2**) $q = 0.96$ (quasiperiodic), (**b1**,**b2**) (Continued)

Figure 4: (continued) $q = 0.975$ (periodic), (**c1**,**c2**) $q = 0.98$ (chaotic spiking), and (**d1**,**d2**) $q = 0.99$ (chaotic bursting). All panels are obtained from the initial condition $(x(0), y(0)) = (1, 1)$, with the final 1000 iterations shown. Within a fractional-order interval of only 0.03, the neuron passes through quasiperiodic, periodic, chaotic spiking, and chaotic bursting regimes, showing that q acts as a highly sensitive control parameter of the firing dynamics.

The values $a = 0.89$, $b = 0.18$, $c = 0.28$, and $k = 0.03$ are those given by Chialvo [8] for the aperiodic bursting regime and are adopted unchanged, so that the integer-order limit of the fractional model reproduces the dynamics of the original map. They carry no direct physiological interpretation: the Chialvo map is a generic excitable model with dimensionless variables, and its correspondence with biology lies in the firing patterns it reproduces rather than in its parameter values.

For further clarification, the qualitative changes in the FO Chialvo dynamics under variation of the fractional order q are investigated in Fig. 5 for two ranges $0.95 \le q \le 1$ and $1 \le q \le 1.4$. In general, $0 < q < 1$ is common for diffusion, relaxation, and memory-dominated processes; $q = 1$ recovers the classical integer-order difference (an ordinary first-order system); $1 < q < 2$ is commonly used for systems that behave between a first-order and a second-order (oscillatory/inertial) system. Fig. 5a1 shows that increasing q over $[0.95, 1]$, while other parameters are fixed at those in Fig. 1, produces a wide variety of behaviors. More clearly, Fig. 5a1 shows that at the beginning of the interval, the dynamics settle onto a fixed point, while increasing $q \gtrsim 0.95$ yields quasiperiodic dynamics followed by low- and then large-amplitude chaos, within which many periodic windows are observable. On the other hand, for $1 < q < 1.4$, Fig. 5b1 reveals that the FO Chialvo neuron tends to behave chaotically, with the amplitude of the attractor increasing monotonically, although many periodic windows are almost undetected. These observations are also verified by the corresponding LLE diagrams in Fig. 5a2,b2.

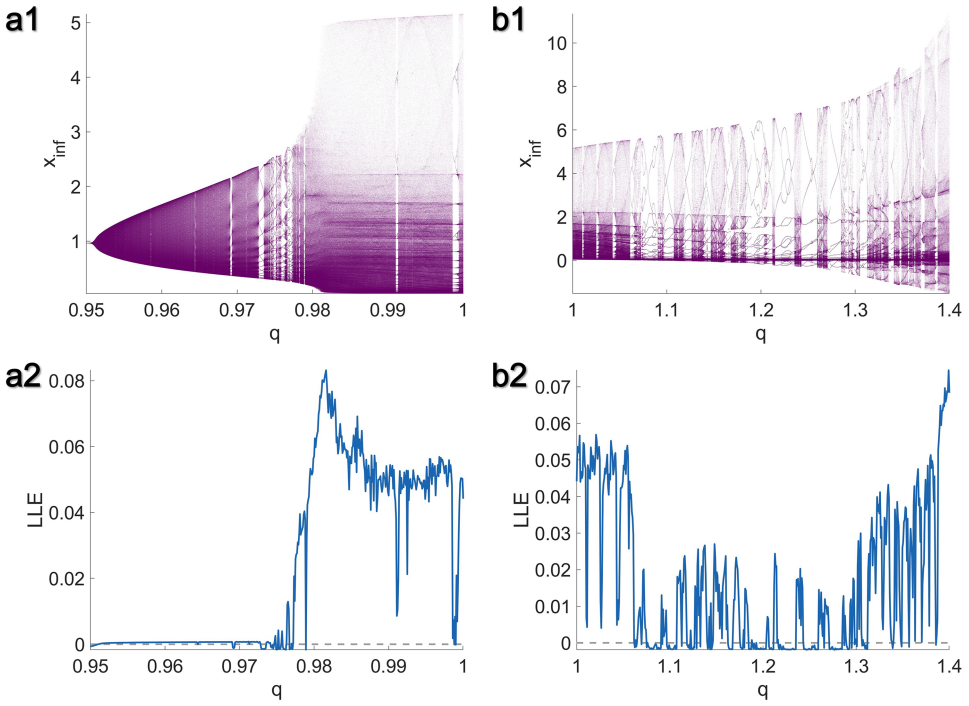


Figure 5: (**a1**,**b1**) The bifurcation and (**a2**,**b2**) LLE diagrams of the FO Chialvo neuron map as a function of the fractional order q for (**a1**,**a2**) $q \in [0.95, 1]$ and (**b1**,**b2**) $q \in [1, 1.4]$, with $a = 0.89$, $b = 0.18$, $c = 0.28$, and $k = 0.03$, obtained from the initial condition $(x(0), y(0)) = (1, 1)$. The dashed line in panels (**a2**,**b2**) marks $LLE = 0$. For $0.95 \le q \le 1$, the neuron passes from a fixed point through quasiperiodicity into chaos, whereas for $1 \le q \le 1.4$, it remains predominantly chaotic and the amplitude of the attractor grows monotonically.

Since the fractional order represents memory-dependent properties in neuronal models, only $0 < q < 1$ is considered in the remaining analyses, and within this range attention is restricted to $0.95 \leq q \leq 1$. As shown in Section 3.1, the equilibrium is asymptotically stable for $q \lesssim 0.951$ and loses stability above this value through a Neimark–Sacker bifurcation, so the interval brackets the critical order, extending from the stable resting state to the integer-order limit; the values $q = 0.96$ (quasiperiodic region in Fig. 5a1), 0.975 (periodic window in Fig. 5a1), 0.98 (small-amplitude chaos in Fig. 5a1), and 0.99 (large-amplitude chaos in) sample it from just above onset to the neighborhood of $q = 1$.

3 Results

This section elaborates on the results of performing stability analysis as well as a comprehensive dynamical analysis of an isolated FO Chialvo neuron model through bifurcation and LE diagrams. Moreover, the collective dynamics of the FO networked model are studied based on the type of coupling function, or so-called synapse in neuroscience.

3.1 Stability Analysis

The first step in investigating the system dynamics is to locate the equilibrium point(s) and determine their stability. For the fractional-order system in Eq. (12), the equilibria are the states at which the right-hand side vanishes, so that

$$\begin{aligned} &(x^*)^{\,2} e^{y^*-x^*} + k - x^* = 0, \\ &a y^* - b x^* + c - y^* = 0. \end{aligned} \tag{15}$$

The second relation is linear in y^* and yields $y^* = \frac{(c-bx^*)}{a-1}$, which, substituted into the first, reduces the problem to a single transcendental equation in x^*,

$$x^* e^{\frac{(c-bx^*)}{a-1}-x^*} + k = 0. \tag{16}$$

Eq. (16) has no closed-form solution and is therefore solved numerically. For the parameter values used throughout this study, $a = 0.89$, $b = 0.18$, $c = 0.28$, and $k = 0.03$, it possesses a single real root, so that the FO Chialvo neuron map has the unique equilibrium $(x^*, y^*) = (0.9634, 0.9691)$. This point lies at the center of the inner spiral visible in the phase portrait of Fig. 1a, about which the subthreshold oscillations of the bursting regime are organized.

The stability of the equilibrium is determined by the eigenvalues (λ_i) of the Jacobian matrix of the right-hand side of Eq. (12), evaluated at

$$J = \begin{bmatrix} (2-x)xe^{y-x} - 1 & x^2 e^{y-x} \\ -b & a-1 \end{bmatrix}. \tag{17}$$

For $0 < q < 1$, the equilibrium of a Caputo-like fractional difference system is asymptotically stable if and only if every eigenvalue λ_i of J satisfies the two conditions [67]:

Condition 1: $|Arg\,(\lambda_i)| > \frac{q\pi}{2}$.

Condition 2: $|\lambda_i| < \left(2\cos\left(\frac{|Arg(\lambda_i)|-\pi}{2-q}\right)\right)^q$.

Evaluating Eq. (17) at (x^*, y^*) yields a complex-conjugate pair,

$\lambda_{1,2} = -0.0528 \pm 0.4059i$, $|\lambda_{1,2}| = 0.4093$, $|Arg\,(\lambda_{1,2})| = 0.5412\pi$.

Condition 1 is satisfied whenever $q < 1.082$ and therefore holds over the entire interval $0 < q < 1$. Condition 2, by contrast, is violated beyond a critical fractional order: the right-hand side of Condition 2 decreases monotonically with q and falls below $|\lambda_{1,2}|$ at $q \approx 0.951$. The equilibrium of the FO Chialvo neuron map is consequently asymptotically stable for $q \lesssim 0.951$ and unstable for $q \gtrsim 0.951$.

Two features of this result deserve emphasis. First, because the destabilizing eigenvalues form a complex-conjugate pair rather than a real one, the loss of stability at $q \approx 0.951$ is of Neimark–Sacker type and gives rise to an invariant circle whose radius grows continuously from zero. This is precisely the behavior observed numerically in Fig. 5a1, where the fixed point persists up to $q \approx 0.95$ and is replaced immediately above it by quasiperiodic motion of gradually increasing amplitude, with the corresponding LLE in Fig. 5a2 remaining at zero throughout that band.

Second, in the integer-order limit $q = 1$, the stability conditions reduce to the classical requirement that the eigenvalues of the map's Jacobian, namely $1 + \lambda_{1.2}$, lie inside the unit circle. Here $|1 + \lambda_{1,2}| = 1.030 > 1$, so the fixed point of the classical Chialvo map is unstable, consistent with the chaotic bursting reported in Fig. 1. The fractional order therefore acts as the parameter that governs the stability of the resting state: strong memory (small q) stabilizes it, while weak memory (q approaching unity) destabilizes it and initiates the transition to oscillatory and ultimately chaotic firing.

3.2 Dynamical Analysis

As shown in Fig. 5, the fractional order significantly affects the neuron's dynamics. Here, therefore, its influence on the same parameter scans is investigated and presented in Fig. 6. Fig. 6a1–a4 correspond to $q = 0.96$, Fig. 6b1–b4 to $q = 0.975$, Fig. 6c1–c4 to $q = 0.98$, and Fig. 6d1–d4 to $q = 0.99$, where panels a1–d1, a2–d2, a3–d3, and a4–d4 respectively show the dynamical variation with respect to $a \in [0.875, 0.915]$ (with $b = 0.18$, $c = 0.28$, and $k = 0.03$), $b \in [0.166, 0.256]$ (with $a = 0.89$, $c = 0.28$, and $k = 0.03$), $c \in [0.25, 0.3]$ ($a = 0.89$, $b = 0.18$, and $k = 0.03$), and $k \in [0.0195, 0.074]$ (with $a = 0.89$, $b = 0.18$, and $c = 0.28$). Compared with Fig. 2a, panels a1–d1 show that the chaotic region contracts toward lower values of a as the fractional order q is reduced, while the quasiperiodic region is preserved but likewise displaced toward lower a. The chaotic band terminates near $a \approx 0.895$ in panel a1 and near $a \approx 0.905$ in panel d1, so that decreasing q shifts the whole regime sequence to the left without altering its order: chaos, quasiperiodicity, fixed point. In every panel of this row, the quasiperiodic lens collapses onto a horizontal branch that persists to the end of the interval, providing a direct numerical counterpart to the stable equilibrium. Moreover, as q decreases, the system increasingly settles onto fixed-point dynamics as a grows.

The same structural pattern is observed for the variation of parameter c (Fig. 6a3–d3) and parameter k (Fig. 6a4–d4). In the former, the end of the chaotic band moves from $c \approx 0.275$ in panel a3 to $c \approx 0.288$ in panel d3, a comparatively modest displacement, so that c is the parameter whose bifurcation structure is most robust to the fractional order. Parameter k, by contrast, is by far the most sensitive: the chaotic region is entirely absent in panel a4, where the dynamics consist solely of a quasiperiodic lens that opens near $k \approx 0.02$, reaches its maximum extent near $k \approx 0.028$, and collapses onto a fixed-point branch at $k \approx 0.037$. As q is increased, a chaotic band emerges and widens progressively across panels b4–d4, extending to $k \approx 0.04$ in panel d4. The fractional order q therefore does not merely displace the regimes along the k axis but determines whether chaotic firing occurs at all within the interval examined.

The bifurcation diagrams for parameter b (Fig. 6a2–d2) are affected by q both in position and in structure. At the beginning of the interval, a shift toward lower values of b is observed as q decreases, whereas at higher values of b the arrangement of periodic windows and chaotic regions, together with the type of transitions between them, changes with q without a systematic pattern. In addition, this row exhibits closed, densely filled loops superposed on the chaotic band at large b, corresponding to quasiperiodic islands. Their

number, size, and location vary irregularly across panels a2–d2, which distinguishes b from the other three parameters, where the fractional order acts almost purely as a translation of the regime sequence.

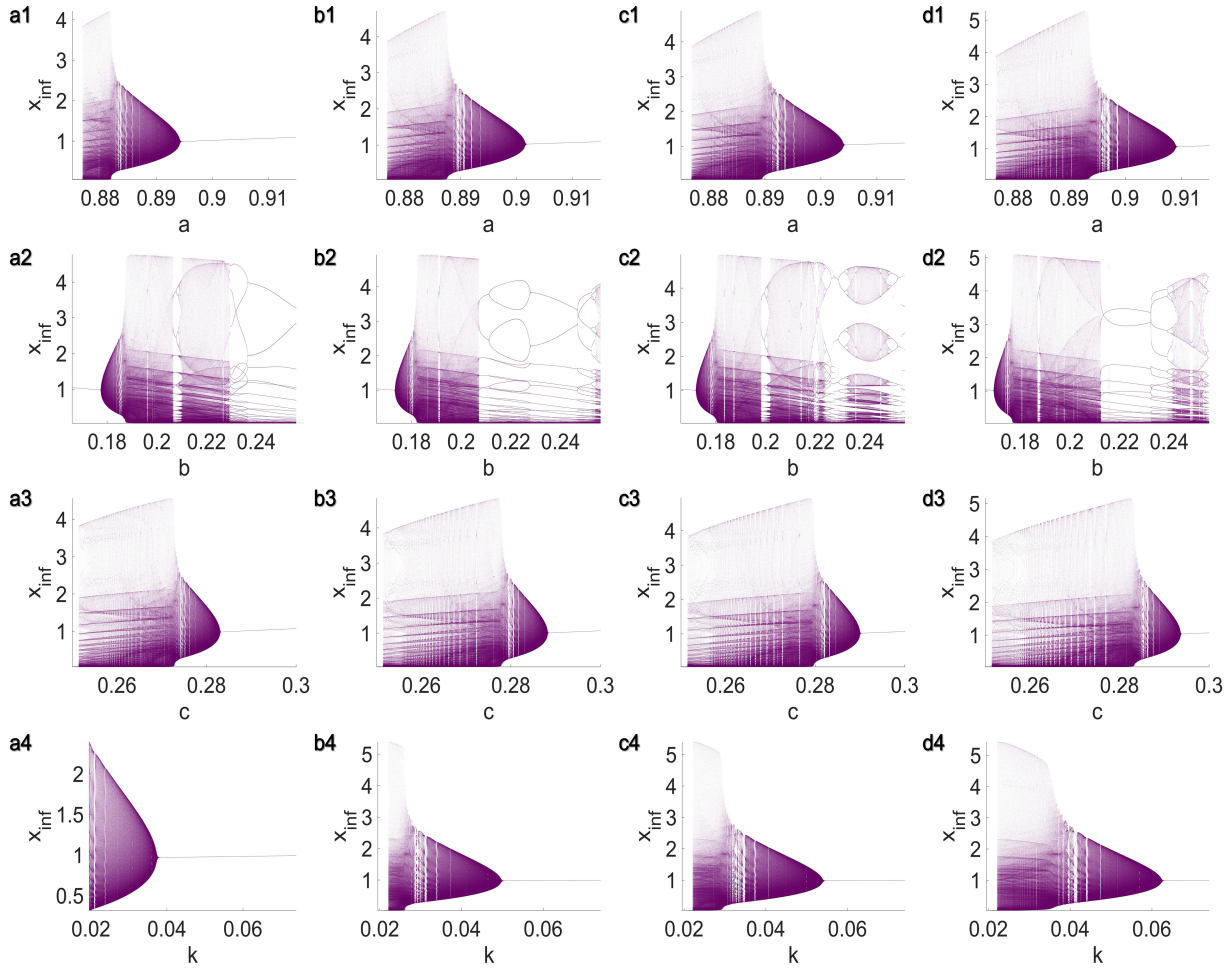


Figure 6: The bifurcation diagrams of the FO Chialvo neuron map as a function of (**a1**–**d1**) parameter a ($a \in [0.875,\ 0.915]$, $b = 0.18$, $c = 0.28$, and $k = 0.03$), (**a2**–**d2**) parameter b ($b \in [0.166,\ 0.256]$, $a = 0.89$, $c = 0.28$, and $k = 0.03$), (**a3**–**d3**) parameter c ($c \in [0.25,\ 0.3]$, $a = 0.89$, $b = 0.18$, and $k = 0.03$), and (**a4**–**d4**) parameter k ($k \in [0.0195,\ 0.074]$, $a = 0.89$, $b = 0.18$, and $c = 0.28$), for (**a1**–**a4**) $q = 0.96$, (**b1**–**b4**) $q = 0.975$, (**c1**–**c4**) $q = 0.98$, (**d1**–**d4**) $q = 0.99$, obtained from the initial condition $(x(0), y(0)) = (1, 1)$. The vertical axis shows the asymptotic values x_{inf} of the activation variable after the transient has been discarded. Decreasing the fractional order shifts the whole regime sequence toward lower parameter values and enlarges the fixed-point region. The effect is strongest for k, where chaos vanishes entirely at the smallest q, and weakest for c.

Overall, as q increases, the bifurcation diagrams become progressively more similar to those of the non-fractional map in Fig. 2, whereas as q decreases, the system tends toward fixed-point behavior over most of the parameter ranges and the remaining dynamical structures shift toward lower parameter values. This is consistent with the stability analysis of Section 3.1. The critical fractional order at which the equilibrium loses stability is determined by the eigenvalues of the Jacobian, which themselves depend on a, b, c, and k. Evaluating the stability conditions along each scan shows that this critical order increases monotonically with a, c, and k, so that for a given fractional order the equilibrium is stable toward the upper end of every interval. Reducing q satisfies the stability conditions over a progressively wider range, which displaces the boundary

toward lower parameter values and enlarges the fixed-point branch, while correspondingly compressing the oscillatory and chaotic regimes. This is precisely the trend displayed in Fig. 6.

The dynamics recognized in Fig. 6 are verified by the LLE diagrams in Fig. 7, which follow the same panel arrangement. In every panel, the LLE is positive throughout the chaotic bands identified in Fig. 6, becomes negative within the periodic windows and across the fixed-point regions, and vanishes in the quasiperiodic regions. Three features deserve attention. First, the chaotic intervals contract and shift toward lower parameter values as q is reduced, in agreement with Fig. 6. Second, the maximum value attained by the LLE increases monotonically with q in all four rows. The fractional order therefore governs not only the extent of the chaotic regions but also the intensity of the chaos within them, with stronger memory producing weaker exponential divergence. Third, panel a4 exhibits no positive values over the entire k interval, confirming that at the smallest fractional order considered, the chaotic regime is absent for this parameter and the dynamics remain quasiperiodic or stationary throughout. Panels c2 and d2 show the converse effect: a second, weaker chaotic region emerges near $b \approx 0.24$ at the larger fractional orders, which is absent at the smaller ones.

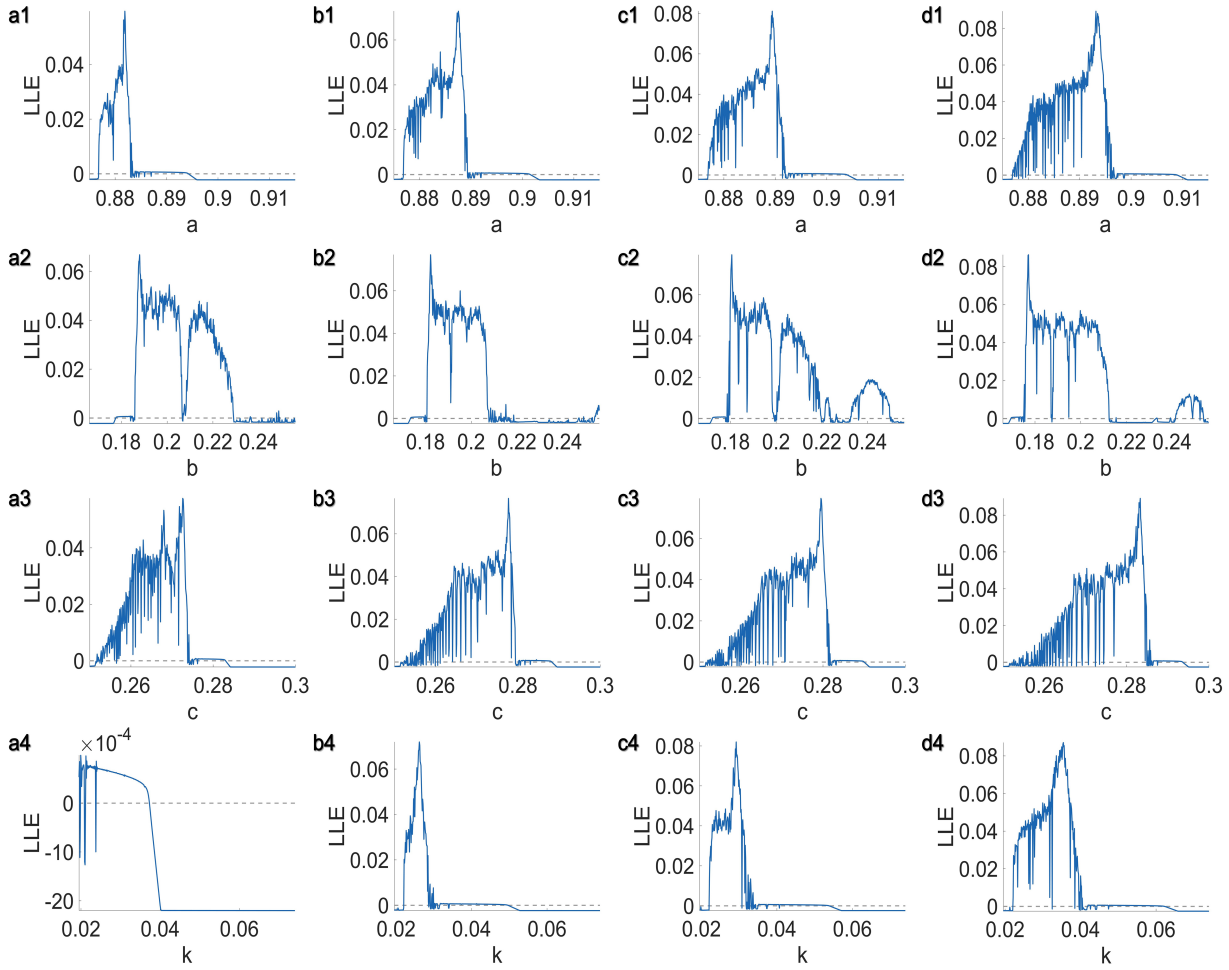


Figure 7: The LLE diagrams of the FO Chialvo neuron map as a function of (**a1**–**d1**) parameter a ($a \in [0.875,\ 0.915]$, $b = 0.18$, $c = 0.28$, and $k = 0.03$), (**a2**–**d2**) parameter b ($b \in [0.166,\ 0.256]$, $a = 0.89$, $c = 0.28$, and $k = 0.03$), (**a3**–**d3**) parameter c ($c \in [0.25,\ 0.3]$, $a = 0.89$, $b = 0.18$, and $k = 0.03$), and (**a4**–**d4**) parameter k ($k \in [0.0195,\ 0.074]$, $a = 0.89$,
(Continued)

Figure 7: (continued) $b = 0.18$, and $c = 0.28$), for (**a1**–**a4**) $q = 0.96$, (**b1**–**b4**) $q = 0.975$, (**c1**–**c4**) $q = 0.98$, (**d1**–**d4**) $q = 0.99$, computed over the same parameter scans as Fig. 6 from the initial condition $(x(0), y(0)) = (1, 1)$. The dashed line marks $LLE = 0$; positive values indicate chaos, zero values quasiperiodicity, and negative values periodic or fixed-point dynamics. The chaotic intervals contract and the maximum LLE decreases as the fractional order is reduced, until at the smallest q the chaotic regime disappears entirely for parameter k (panel a4).

Fig. 8 shows the simultaneous effect of the fractional order and the parameter variation through two-dimensional bifurcation diagrams in the a–q (Fig. 8a), b–q (Fig. 8b), c–q (Fig. 8c), and k–q (Fig. 8d) planes, in which the dynamics are coded in pink (chaotic), cyan (quasiperiodic), yellow (periodic), and gray (fixed point). The remaining parameters are fixed at the values used in Figs. 6 and 7, and the fractional order is varied over $0.95 \leq q \leq 1$.

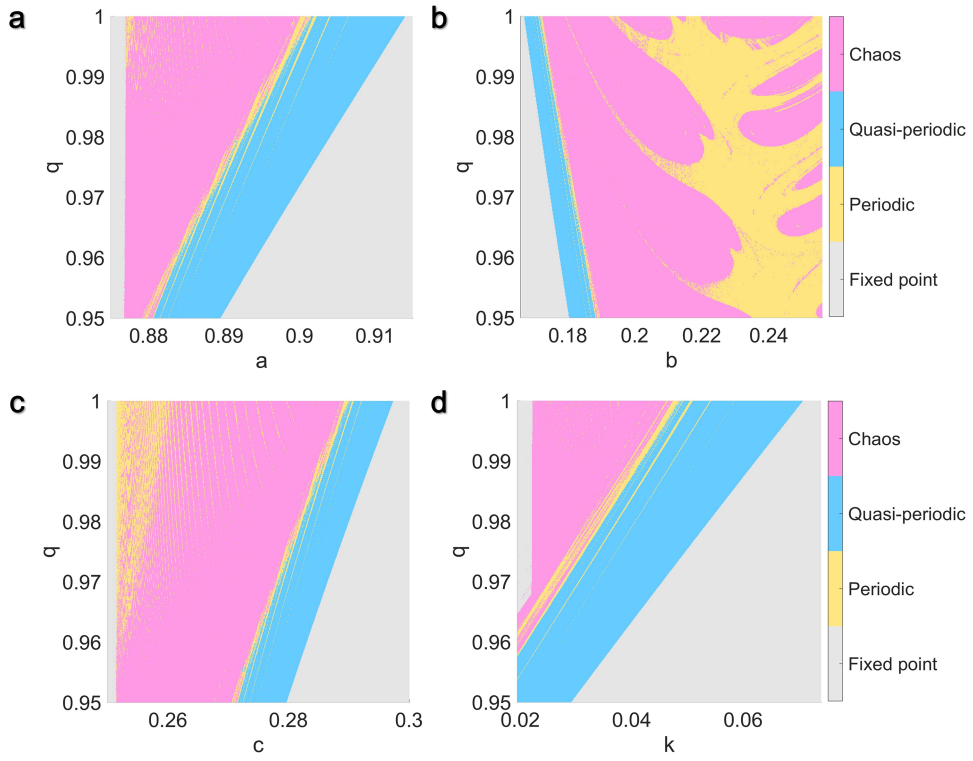


Figure 8: The two-dimensional bifurcation diagrams of the FO Chialvo neuron in the plane of the fractional order q ($0.95 \leq q \leq 1$) and (**a**) parameter a ($a \in [0.875,\ 0.915]$, $b = 0.18$, $c = 0.28$, and $k = 0.03$), (**b**) parameter b ($b \in [0.166,\ 0.256]$, $a = 0.89$, $c = 0.28$, and $k = 0.03$), (**c**) parameter c ($c \in [0.25,\ 0.3]$, $a = 0.89$, $b = 0.18$, and $k = 0.03$), and (**d**) parameter k ($k \in [0.0195,\ 0.074]$, $a = 0.89$, $b = 0.18$, and $c = 0.28$), obtained from the initial condition $(x(0), y(0)) = (1, 1)$. Chaotic, quasiperiodic, periodic, and fixed-point dynamics are shown in pink, cyan, yellow, and gray, respectively. In panels (**a**,**c**,**d**), the regime boundaries are close to straight lines of positive slope, and the interface between the quasiperiodic and fixed-point regions coincides with the Neimark–Sacker curve; in panel (**b**), the ordering of the regimes is reversed, and the boundaries are strongly irregular.

Fig. 8a,c,d shares a common organization. Along any horizontal line, the four regimes appear in the same order—chaos, narrow periodic bands, quasiperiodicity, and finally the fixed point as the control parameter increases—and the boundaries separating them are close to straight lines of positive slope. The critical parameter value at which each transition occurs therefore grows almost linearly with q, so that reducing the fractional order displaces the entire regime sequence toward lower parameter values. The

boundary between the quasiperiodic and fixed-point regions is of particular interest, since it is the locus of the Neimark–Sacker bifurcation identified in Section 3.1. Evaluating Conditions 1 and 2 along each scan places this boundary at $a \approx 0.8895$, $c \approx 0.2797$, and $k \approx 0.0292$ for $q = 0.95$, and at $a \approx 0.9140$, $c \approx 0.2974$, and $k \approx 0.0709$ for $q = 1$, in agreement with the interfaces observed in panels a, c, and d. The displacement of the boundary across this interval is far larger for k. This quantifies the greater sensitivity of the k dynamics to the fractional order analytically already apparent in Figs. 6 and 7. The panels differ markedly in the relative extent of the four regimes. In panel d, the fixed-point region occupies the greater part of the plane and the chaotic region is confined to a narrow wedge at small k that vanishes below $q \approx 0.96$, which is the two-dimensional counterpart of the absence of chaos observed in Figs. 6a4 and 7a4. In panel c, by contrast, chaos dominates the left half of the plane and is finely interleaved with periodic windows appearing as dense yellow striations. Panel a is intermediate between these two cases.

Panel b differs from the others in both the ordering and the geometry of the regimes. Moving toward larger b, the sequence runs from the fixed point through a narrow quasiperiodic band into chaos and finally into an extended periodic region—the reverse of the ordering found in panels a, c, and d. This reversal has a direct analytical counterpart: the Neimark–Sacker boundary obtained from Conditions 1 and 2 lies at $b \approx 0.1803$ for $q = 0.95$ and at $b \approx 0.1669$ for $q = 1$, so that it migrates toward lower parameter values as the fractional order increases, whereas in the other three scans it migrates toward higher ones. The fixed-point region consequently forms a narrow wedge along the left edge of the plane that tapers as q approaches unity, rather than the broad triangle occupying the lower-right portion of panels a, c, and d. The chaotic region is likewise bounded on both sides in b, being confined between the quasiperiodic band near $b \approx 0.18$ and the onset of the periodic region near $b \approx 0.21$, whereas in the remaining panels chaos extends to the edge of the scanned interval. Beyond $b \approx 0.21$ the periodic region penetrates the chaotic one as a set of lobed tongues whose size and position vary irregularly with q, and isolated chaotic islands persist within the periodic domain up to the largest values of b considered. It is notable that, although the global organization of panel b is by far the most sensitive to the fractional order, the displacement of its stability boundary is the smallest of the four. The fractional order therefore acts on b principally through the structure of the chaotic and periodic regions rather than through the stability of the resting state. This confirms in two dimensions the structural distinction between b and the remaining parameters noted in the discussion of Fig. 6.

3.3 Synchronization

For further investigation, the synchronization of $N = 100$ globally coupled FO Chialvo neuron maps is explored here under three coupling schemes: electrical, inner-linking, and chemical.

The electrical coupling function is a linear diffusive function of the variable x. Accordingly, the equations of the i-th neuron of the FO Chialvo network read

$$\begin{aligned} x_i(n) = x_i(0) + \frac{1}{\Gamma(q)} \sum_{l=1}^{n} \frac{\Gamma(n-l+q)}{\Gamma(n-l+1)} \Big(& x_i^2(l-1)\, e^{y_i(l-1)-x_i(l-1)} + k - x_i(l-1) \\ & + \sigma_e \sum_{\substack{j=1 \\ j \neq i}}^{N} \big[x_j(l-1) - x_i(l-1) \big] \Big), \\ y_i(n) = y_i(0) + \frac{1}{\Gamma(q)} \sum_{l=1}^{n} \frac{\Gamma(n-l+q)}{\Gamma(n-l+1)} & \Big(a y_i(l-1) - b x_i(l-1) + c - y_i(l-1) \Big), \end{aligned} \tag{18}$$

where σ_e is the electrical coupling strength.

The electrical coupling function can be considered in a more general form, called the inner-linking function, which is likewise diffusive but acts on a nonlinear function of the state rather than on x alone. Through the inner-linking function, Network (18) becomes

$$\begin{aligned} x_i(n) &= x_i(0) + \frac{1}{\Gamma(q)} \sum_{l=1}^{n} \frac{\Gamma(n-l+q)}{\Gamma(n-l+1)} \Big(x_i^2(l-1)\, e^{y_i(l-1)-x_i(l-1)} + k - x_i(l-1) \\ &\quad + \sigma_i \sum_{\substack{j=1 \\ j\neq i}}^{N} \left[f\left(x_j(l-1), y_j(l-1)\right) - f\left(x_i(l-1), y_i(l-1)\right) \right] \Big), \\ y_i(n) &= y_i(0) + \frac{1}{\Gamma(q)} \sum_{l=1}^{n} \frac{\Gamma(n-l+q)}{\Gamma(n-l+1)} \Big(a y_i(l-1) - b x_i(l-1) + c - y_i(l-1) \Big), \end{aligned} \tag{19}$$

where $f\left(x(n), y(n)\right) = x^2(n)\, e^{y(n)-x(n)} + k - x(n)$ and σ_i is the inner-linking strength.

The inner-linking function specifies which combination of state variables is exchanged between coupled units, the electrical coupling of Network (18) being the particular case in which it reduces to the identity. Its use in map-based neuron networks is well established [63,65]. For map-based models, the form of the diffusive coupling rather than its diffusive character alone therefore governs whether chaotic units can be synchronized, and the scheme is included here to determine whether this distinction persists when memory is introduced through the fractional order. The function adopted is the nonlinear part of the activation equation of the map itself, so that no functional form and no parameter beyond the coupling strength σ_i is introduced.

Unlike the electrical and inner-linking functions, chemical coupling is fully nonlinear and can model short- and long-range neuronal connections. The $N = 100$ globally coupled FO Chialvo neuron maps connected via a chemical coupling function are described by

$$\begin{aligned} x_i(n) &= x_i(0) + \frac{1}{\Gamma(q)} \sum_{l=1}^{n} \frac{\Gamma(n-l+q)}{\Gamma(n-l+1)} \Big(x_i^2(l-1)\, e^{y_i(l-1)-x_i(l-1)} + k - x_i(l-1) \\ &\quad + \sigma_c \left(v_s - x_i(l-1)\right) \sum_{\substack{j=1 \\ j\neq i}}^{N} \Gamma\left(x_j(l-1)\right) \Big), \\ y_i(n) &= y_i(0) + \frac{1}{\Gamma(q)} \sum_{l=1}^{n} \frac{\Gamma(n-l+q)}{\Gamma(n-l+1)} \Big(a y_i(l-1) - b x_i(l-1) + c - y_i(l-1) \Big), \end{aligned} \tag{20}$$

where $\Gamma\left(x(n)\right) = \left(1 + e^{-r(x(n)-\Theta_s)}\right)^{-1}$ is the synaptic activation function, $r = 50$ is its steepness, $\Theta_s = -1.4$ is the synaptic threshold, $v_s = -1.4$ is the reversal potential, and σ_c is the chemical coupling strength.

To assess the synchronization, time-averaged synchronization error E and the order parameter R are employed. In this case, where N neurons are considered, E and R can be obtained through

$$E = \left\langle \frac{1}{N-1} \sum_{j=2}^{N} \sqrt{\left(x_j(n) - x_1(n)\right)^2 + \left(y_j(n) - y_1(n)\right)^2} \right\rangle_n, \tag{21}$$

and

$$R = \left\langle \frac{1}{N} \sum_{j=1}^{N} \left| e^{i\left(\frac{2\pi\left(n-n_{j,m}\right)}{n_{j,m+1}-n_{j,m}}\right)} \right| \right\rangle_n, \tag{22}$$

where $\langle \ldots \rangle$ denotes averaging over n iterations and $n_{j,m}$ refers to the onset of m-th spike of the j-th neuron. Since $0 \leq R \leq 1$, the higher value of R indicates greater phase coherence, and $R = 1$ corresponds to complete phase synchrony. Similarly, $E \geq 0$, with lower values denoting stronger synchronization; $E = 0$ corresponds to the complete synchronization state.

Table 1 summarizes the parameters of the FO Chialvo neuron model and the network configurations investigated in this study.

Table 1: Parameters of the FO Chialvo neuron model with the coupling schemes.

Model	Symbol	Description	Value
Neuron	a	Recovery time constant	0.89
	b	Dependence of the recovery state on the activation	0.18
	c	Offset	0.28
	k	Bias (additive perturbation)	0.03
	q	Fractional order	$[0.95, 1]$
Network	N	Number of neurons	100
	σ_e	Electrical coupling strength	$[0, 0.002]$
	σ_i	Inner-linking coupling strength	$[0, 0.002]$
	σ_c	Chemical coupling strength	$[0, 0.002]$
	v_s	Synaptic reversal potential	−1.4
	Θ_s	Synaptic threshold	−1.4
	r	Steepness of the synaptic activation function $\Gamma(x)$	50

Fig. 9 shows E (panels a1–a3) and R (panels b1–b3) obtained for Network (18) (Fig. 9a1,b1), Network (19) (Fig. 9a2,b2), and Network (20) (Fig. 9a3,b3) in the σ-q plane ($0 \leq \sigma \leq 0.002$ and $0.95 \leq q \leq 1$). Panels c1–c3 present E and R as functions of the electrical (Fig. 9c1), inner-linking (Fig. 9c2), and chemical (Fig. 9c3) coupling strengths over the same interval at $q = 0.98$. The remaining parameters are set as listed in Table 1. In all three cases, complete synchronization is achieved over a considerable region of the parameter space.

Under electrical coupling, neurons synchronize as σ_e increases, with the onset of synchronization displaced toward higher coupling strengths at higher fractional orders. For low q, the synchronous state is reached almost immediately, at the very beginning of the σ_e interval, whereas at intermediate q synchronization is suppressed within a small region embedded in the otherwise synchronous domain. Under inner-linking coupling, this suppression is absent, and synchronization is attained at the very beginning of the σ_e interval for small and intermediate q. In both schemes, synchronization remains achievable at large q provided the coupling strength is increased, but its onset occurs at lower coupling under inner-linking than under electrical coupling.

Since both the electrical and the inner-linking functions are diffusive, the coupling term vanishes on the synchronization manifold where $x_1(n) = \ldots, x_N(n)$ and $y_1(n) = \ldots, y_N(n)$, so that in the synchronous state ($E = 0$) the network follows the dynamics of the isolated neuron characterized in Section 3.2. This accounts for the dependence of the synchronization onset on q: at low fractional orders, the isolated neuron rests at a fixed point or on a periodic/quasiperiodic attractor, and a negligible coupling strength suffices to bring the network onto it, whereas synchronizing chaotic motion at higher q requires substantially stronger coupling.

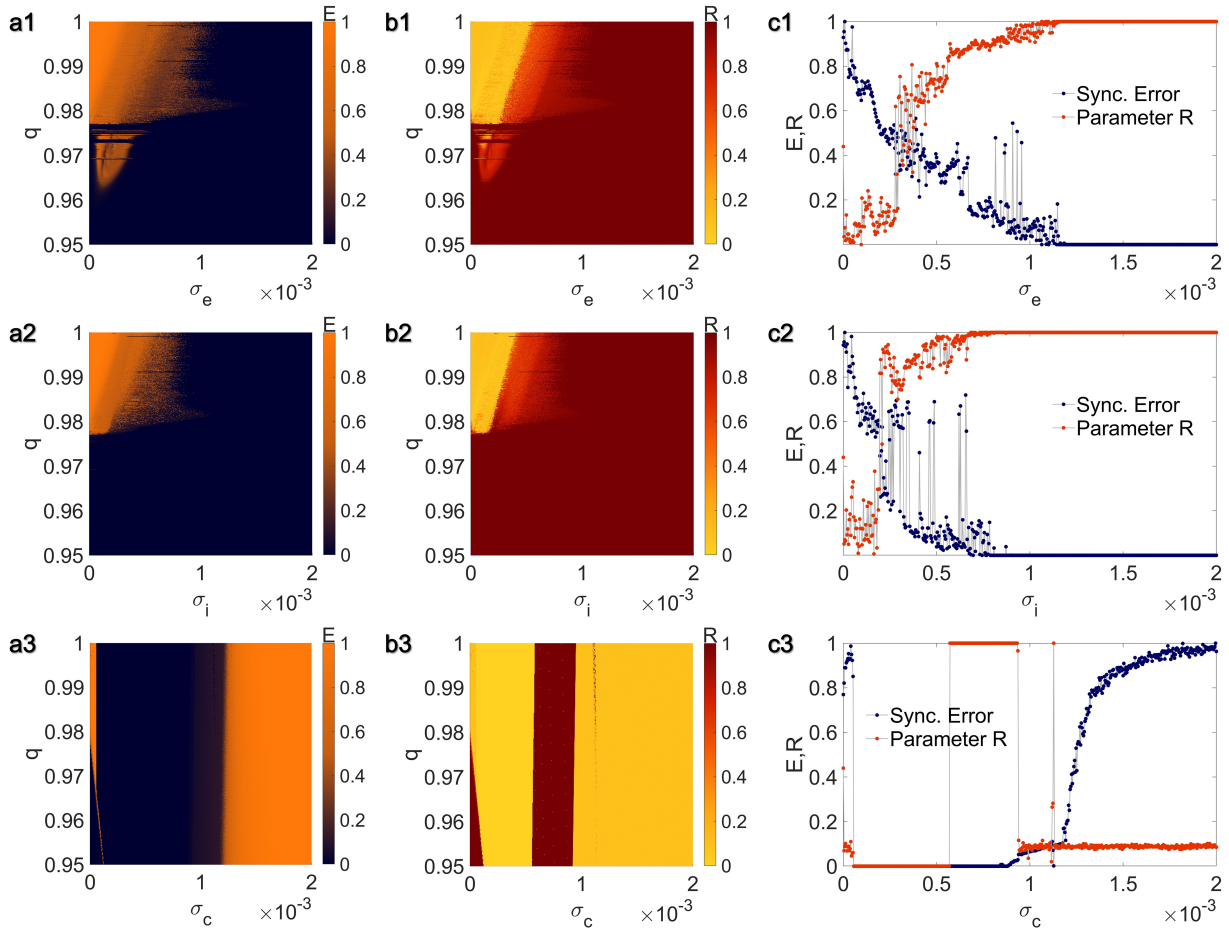


Figure 9: (**a1**–**a3**) The time-averaged synchronization error E and (**b1**–**b3**) the order parameter R in q-σ plane ($0.95 \leq q \leq 1$, $0 \leq \sigma_e, \sigma_i, \sigma_c \leq 0.002$) and as a function of σ for $q = 0.98$ obtained for $N = 100$ FO Chialvo neuron maps coupled via (**a1**–**c1**) electrical, (**a2**–**c2**) inner-linking, and (**a3**–**c3**) chemical coupling functions. The model parameters are set to $a = 0.89$, $b = 0.18$, $c = 0.28$, and $k = 0.03$. Complete synchronization is attained under all three coupling schemes, at lower coupling strengths for inner-linking than for electrical coupling, while chemical coupling additionally produces a region of synchronized oscillation death.

Under chemical coupling, the picture differs. The neurons behave asynchronously at both very small and very large σ_c, and synchronization is confined to an intermediate band. As q decreases toward 0.95, the narrow asynchronous region at small σ_c contracts into a thin separator, beyond which the synchronous region extends from the very beginning of the σ_c interval. Within the synchronous domain, a subregion is observed in which $R \approx 0$ while $E \approx 0$, indicating that the neurons converge to a common quiescent state rather than to a common oscillation—that is, to synchronized oscillation death. Since the chemical coupling term does not vanish on the synchronization manifold, the synchronous dynamics under this scheme differ from those of the isolated neuron and warrant further investigation.

Finally, panels c1 and c2 show no pure phase synchronization: R reaches unity only where E vanishes, so that phase coherence and complete synchronization set in together. In contrast, panel c3 exhibits a narrow interval near $\sigma_c \approx 0.0009$ in which $R \approx 1$ while E remains non-zero, indicating that chemically coupled neurons can lock in phase without achieving complete synchronization.

Focusing on the transitions to synchrony in Fig. 9c1, Fig. 10 shows the collective dynamics of FO neurons connected through electrical synapses for σ_e = 0.000116 (Fig. 10a1–c1), σ_e = 0.0008 (Fig. 10a2–c2), and σ_e = 0.0011 (Fig. 10a3–c3), where panels a1–a3 show the spatiotemporal patterns, panels b1–b3 the time series, and panels c1–c3 the phase-space trajectories. At the smallest coupling strength, the network organizes into two clusters, within each of which the neurons are synchronized on a periodic solution—a state known as cluster synchronization. The two clusters follow the same closed orbit in phase space (Fig. 10c1), but are separated in phase, producing the alternating pattern in the spatiotemporal diagram in Fig. 10a1. The clusters are moreover in an antiphase state, with a phase difference of half a period.

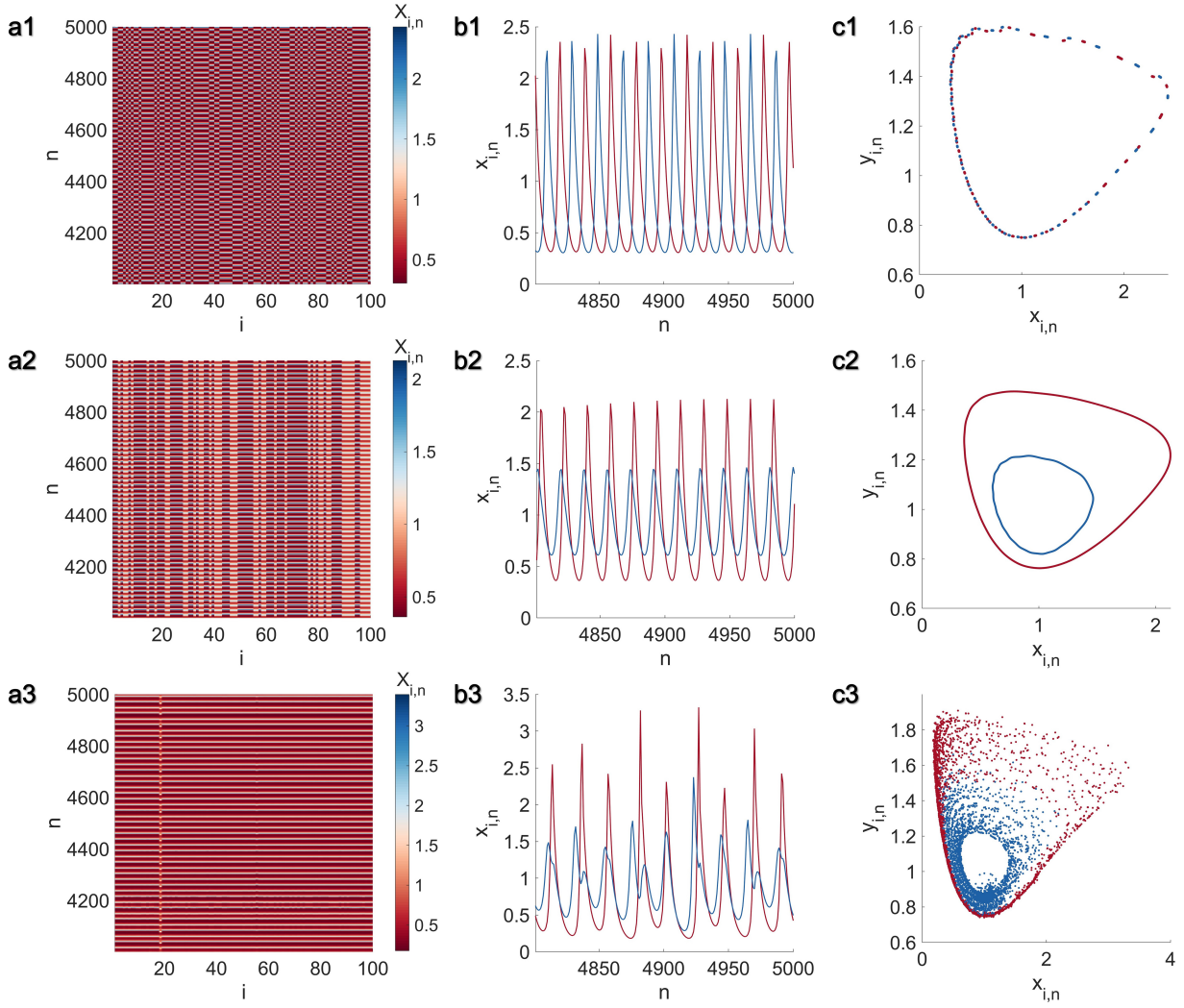


Figure 10: (**a1**–**a3**) The spatiotemporal pattern, (**b1**–**b3**) the time series, and (**c1**–**c3**) the phase-space trajectories of N = 100 globally coupled FO Chialvo neurons connected via the electrical coupling function. The model parameters are set to a = 0.89, b = 0.18, c = 0.28, and k = 0.03 with q = 0.98, and (**a1**–**c1**) σ_e = 0.000116, (**a2**–**c2**) σ_e = 0.0008, and (**a3**–**c3**) σ_e = 0.0011. With increasing coupling strength, the network passes from two-cluster synchronization on a common periodic orbit, through cluster synchronization on two distinct quasiperiodic orbits, to a solitary state in which all neurons but one share a common chaotic attractor.

Similarly, Fig. 11, which follows the same panel arrangement, shows that at σ_i = 0.000067 (Fig. 11a1–c1), the FO neurons achieve cluster synchronization on a periodic solution, as in Fig. 10a1–c1, although here the

two cluster manifolds are of almost identical size. As the coupling strength increases to $\sigma_i = 0.00012$, the same organization persists, but on quasiperiodic dynamics the two manifolds again nearly coincide (Fig. 11c2). In both cases, the red and blue clusters are mutually antiphase, their spikes alternating with a phase difference of half a period. A further increase to $\sigma_i = 0.00041$ leaves all neurons but six synchronized on a large-amplitude chaotic manifold (red in Fig. 11c3), while the remaining six occupy three low-amplitude chaotic manifolds and appear in Fig. 11a3 as six isolated columns interrupting the otherwise uniform spatiotemporal pattern.

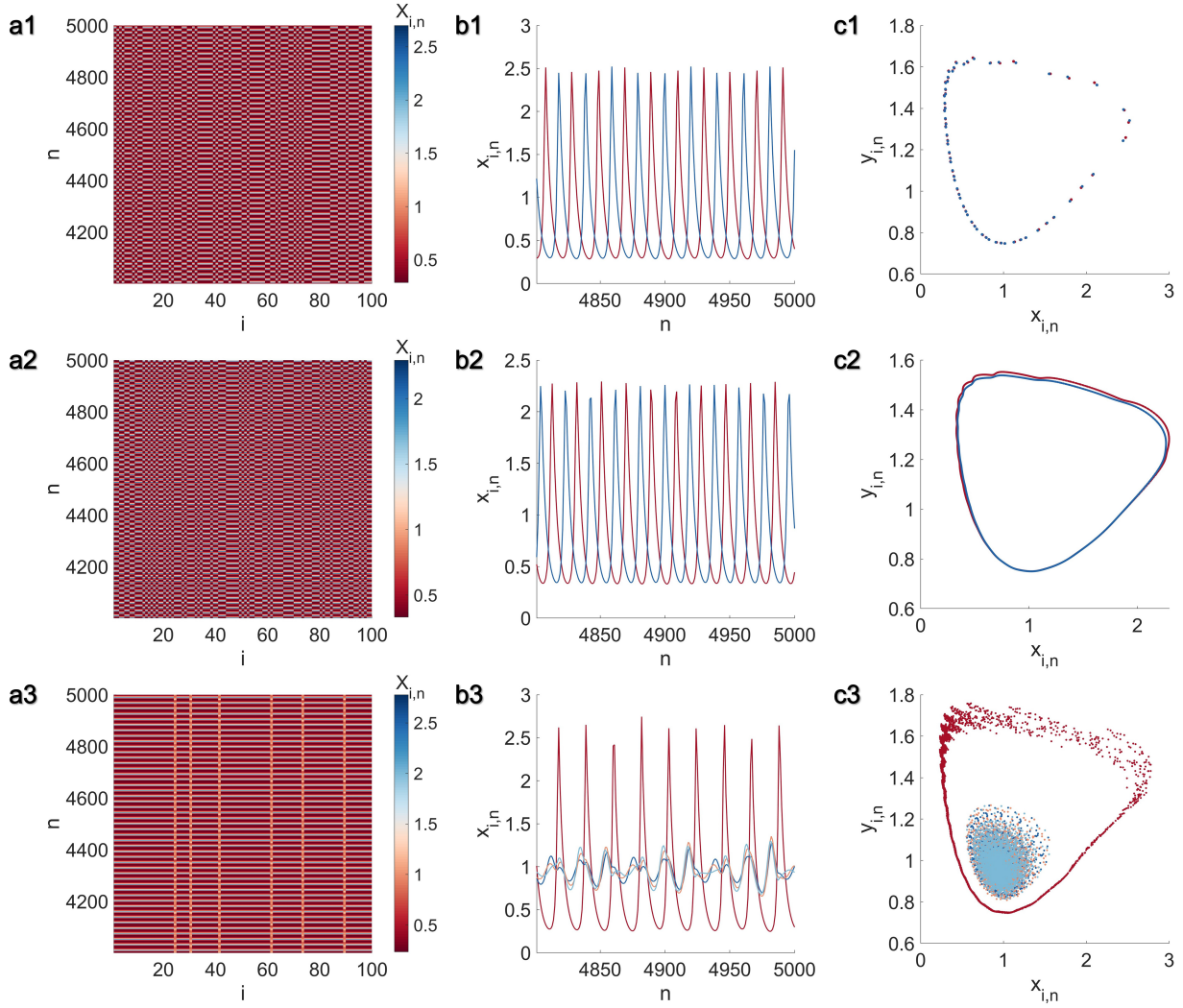


Figure 11: (**a1**–**a3**) The spatiotemporal pattern, (**b1**–**b3**) the time series, and (**c1**–**c3**) the phase-space trajectories of N = 100 globally coupled FO Chialvo neurons connected via the inner-linking coupling function. The model parameters are set to $a = 0.89$, $b = 0.18$, $c = 0.28$, and $k = 0.03$ with $q = 0.98$, and (**a1**–**c1**) $\sigma_i = 0.000067$, (**a2**–**c2**) $\sigma_i = 0.00012$, and (**a3**–**c3**) $\sigma_i = 0.00041$. With increasing coupling strength, the network passes from two-cluster synchronization on a common periodic orbit, through cluster synchronization on two distinct quasiperiodic orbits, to solitary states in which all neurons but six share a common chaotic attractor.

Investigation of chemically coupled FO Chialvo neurons shows that the neurons behave asynchronously, except within the regions of phase and complete synchrony identified in Fig. 9. With the same panel configuration, Fig. 12a1–c1 and Fig. 12a2–c2, respectively, demonstrate complete synchronization on high-frequency period-2 and period-4 attractors for $\sigma_c = 0.0007$ and $\sigma_c = 0.00085$; the corresponding phase

portraits consist of exactly two and four points (Fig. 12c1,c2). Fig. 12a3–c3 shows phase synchronization at σ_c = 0.00091, where the dynamics of the neurons are chaotic, and the attractor consists of two disjoint bands (Fig. 12c3). The three cases therefore trace a period-doubling route to chaos as the chemical coupling strength increases.

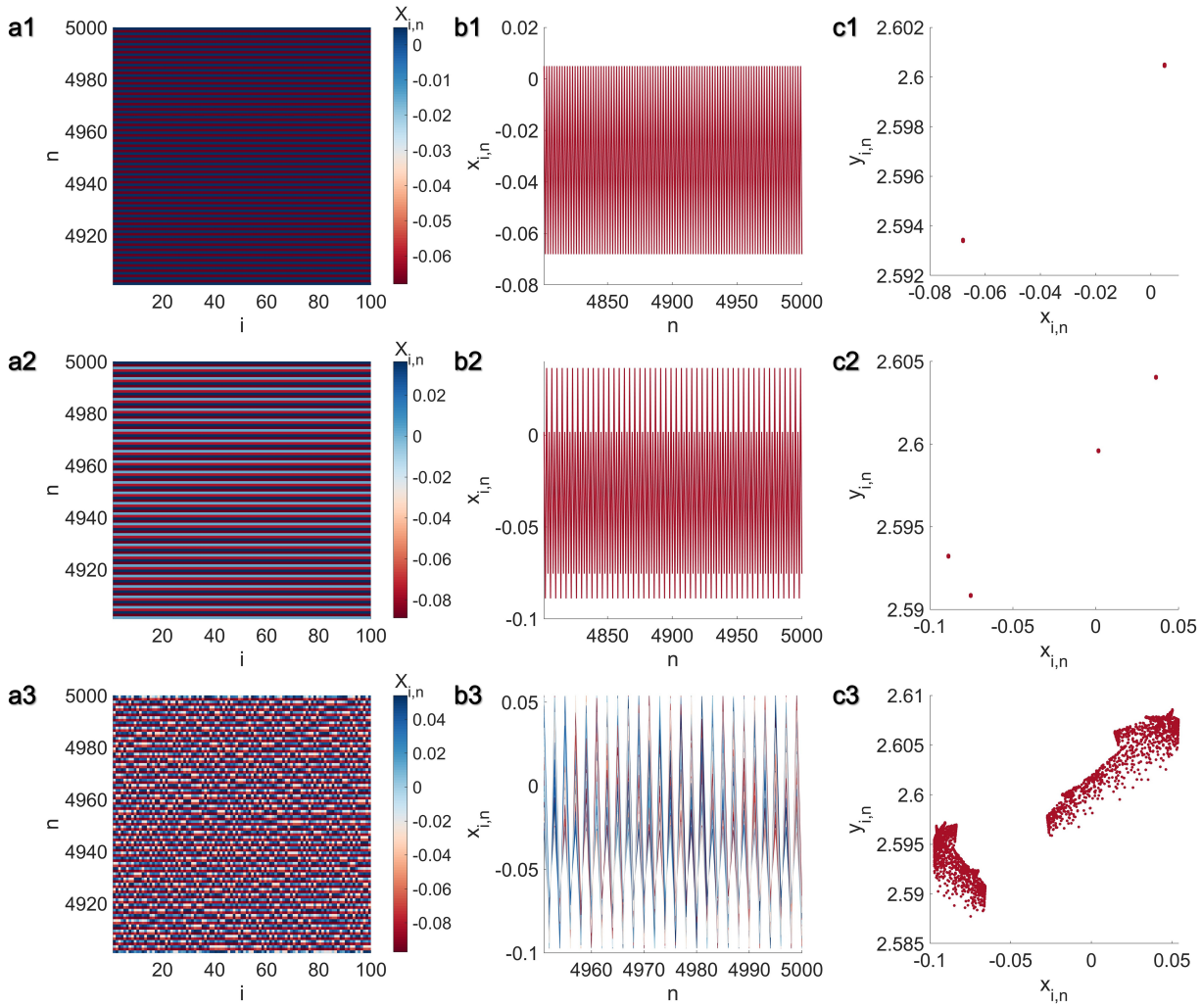


Figure 12: (**a1**–**a3**) The spatiotemporal pattern, (**b1**–**b3**) the time series, and (**c1**–**c3**) the phase-space trajectories of N = 100 globally coupled FO Chialvo neurons connected via the chemical coupling function. The model parameters are set to a = 0.89, b = 0.18, c = 0.28, and k = 0.03 with q = 0.98, and (**a1**–**c1**) σ_c = 0.0007, (**a2**–**c2**) σ_c = 0.00085, and (**a3**–**c3**) σ_c = 0.00091. Increasing the coupling strength produces a period-doubling route on the synchronization manifold, from complete synchronization on a period-2 attractor, through a period-4 attractor, to phase synchronization on a two-band chaotic attractor. In all three cases, the synchronous state occupies a region of the phase plane distinct from that of the isolated neuron.

In all cases, the synchronization manifold differs markedly from the dynamics of the isolated neuron at the same fractional order: the synchronous state remains confined to $x \in [-0.1, 0.05]$ and $y \approx 2.59$–2.61, whereas the uncoupled neuron evolves over a far broader region of the phase plane. This is a direct consequence of the chemical coupling being non-diffusive, so that the coupling term does not vanish on the synchronization manifold.

Figs. 10–12 further reveal that, although no coexisting attractors were found for the isolated FO Chialvo neuron within the parameter and initial-condition ranges examined, the networked model can support several distinct dynamical states simultaneously. Under the diffusive coupling schemes—electrical and inner-linking—the units organize into clusters that follow different orbits at the same parameter values, and in the solitary states of Figs. 10c3 and 11c3, a small number of neurons occupy a low-amplitude chaotic attractor while the remainder share a large-amplitude one. Under chemical coupling, no such coexistence is observed, all neurons sharing a single attractor in each of the cases shown in Fig. 12.

3.4 Extreme Events

Extreme events are rare, recurrent, and disproportionately large fluctuations in the dynamics of a system, whose amplitudes greatly exceed those of typical events [47,48]. As discussed in Section 3.3, the dynamics of the synchronization state of Network (20), in which the FO Chialvo neurons are connected chemically, depend not only on the fractional order and the model parameters but also on the network parameters, and specifically on the coupling strength σ_c. Here, therefore, this dependence is investigated through bifurcation analysis and, at the same time, the possibility of extreme events is examined.

To identify extreme events, a qualifying threshold is defined as

$$T_i = \mu_{x_i} + 8\sigma_{x_i}, \tag{23}$$

where μ_{x_i} and σ_{x_i} denote the sample mean and standard deviation of the local maxima of the variable x of the i-th neuron, evaluated over $n = 100{,}000$ iterations after the transient has been discarded. Any spike of the i-th neuron exceeding T_i is counted as an extreme event.

Fig. 13a shows the regions of the σ_c–q plane, in which extreme events are detected. Their occurrence is confined to a narrow band of coupling strength near $\sigma_c \approx 0.0012$ and is essentially independent of the fractional order, extending across the entire range $0.95 \leq q \leq 1$. Elsewhere in the plane, no spike of any neuron exceeds its qualifying threshold. The origin of this band is clarified by Fig. 13b, which superimposes the threshold on the bifurcation diagram of the first neuron as a function of σ_c. Below $\sigma_c \approx 0.0012$, the network is completely synchronized, and the attractor remains confined to small amplitudes, so that the threshold lies far above the accessible values of $x_{1,inf}$. At $\sigma_c \approx 0.0012$, the attractor expands abruptly, and within the narrow interval over which this expansion takes place the distribution of local maxima acquires a heavy tail: a small number of spikes exceed T_1 and are registered as extreme events. Beyond the transition, the threshold has adjusted to the enlarged attractor, and the events cease.

Extreme events in the chemically coupled FO Chialvo network therefore arise only at the onset of desynchronization identified in Fig. 9a3, and not within the asynchronous regime itself. Thus, the coupling strength is identified as the controlling parameter in the networked case.

Fig. 14 shows the time series of the first neuron of the chemically coupled network within the extreme-event band identified in Fig. 13, for four values of the fractional order and $\sigma_c = 0.0012$. In every case, the dynamics consist of a low-amplitude background interrupted by rare, isolated spikes whose amplitude exceeds that of the background by more than an order of magnitude; a subset of these spikes crosses the qualifying threshold T_1 and is therefore classified as an extreme event.

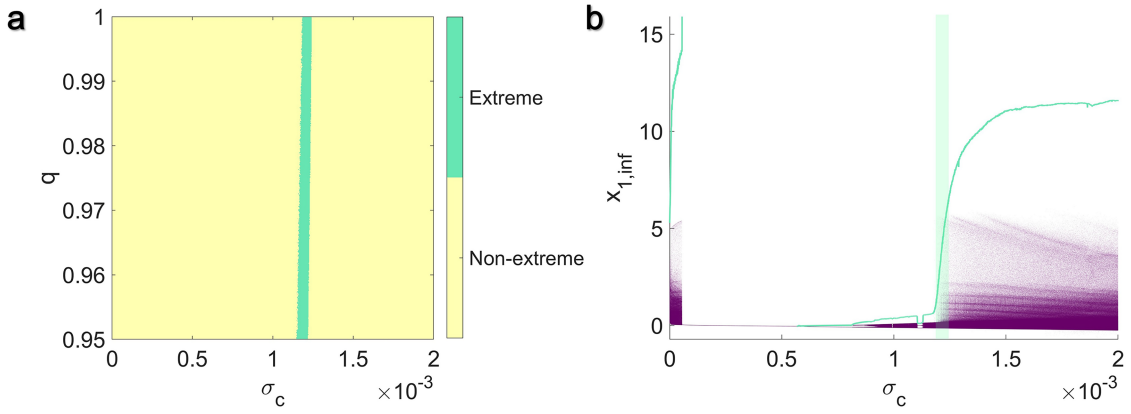


Figure 13: (**a**) The regions of the occurrence of extreme events (shown in green) in σ_c-q space for $0.95 \leq q \leq 1$ and $0 \leq \sigma_c \leq 0.002$. (**b**) The bifurcation diagrams of $N = 100$ FO Chialvo network as a function of σ_c ($\sigma_c \in [0,\ 0.002]$ $a = 0.89$, $b = 0.18$, $c = 0.28$, and $k = 0.03$) with $q = 0.98$, along with the T_1 threshold as the green solid line. The region of σ_c where extreme events are detected is demonstrated in transparent green. The vertical axis shows the asymptotic values x_{inf} of the first neuron's activation variable after the transient has been discarded. Extreme events are confined to a narrow band of coupling strength near $\sigma_c \approx 0.0012$, essentially independent of the fractional order, and coincide with the abrupt expansion of the attractor that marks the onset of desynchronization.

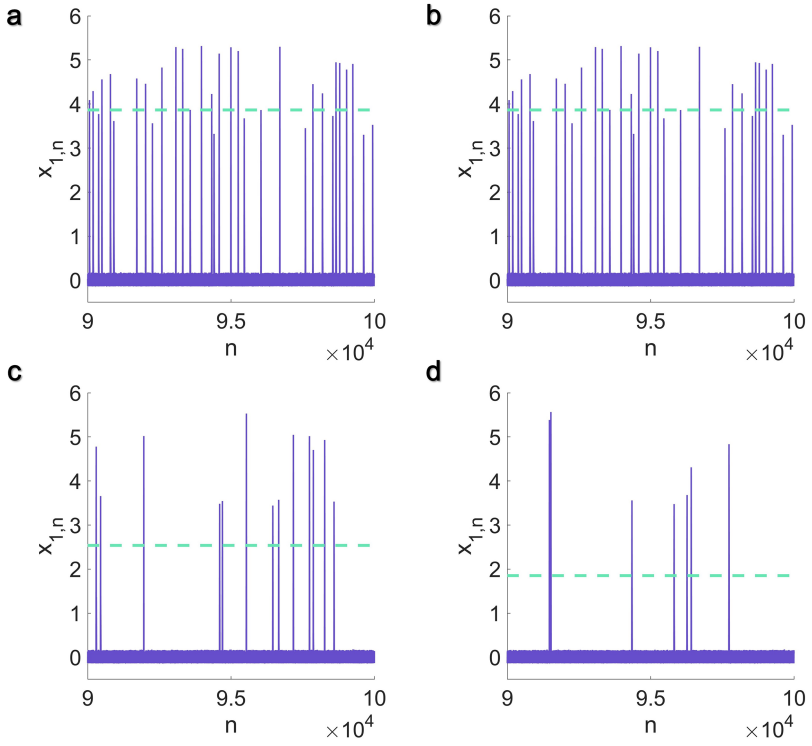


Figure 14: The time series of the first neuron in a network of $N = 100$ chemically coupled FO Chialvo maps described by Network (20), with $\sigma_c = 0.0012$, for (**a**) $q = 0.96$, (**b**) $q = 0.975$, (**c**) $q = 0.98$, and (**d**) $q = 0.99$. The green dashed line represents the qualifying threshold T_1. Extreme events occur at every fractional order shown, but as q increases, the spikes become less frequent and the threshold lower, so that a larger fraction of the spikes qualify as extreme.

The fractional order q controls both the frequency of the spikes and the threshold level. As q increases from 0.96 to 0.99, the number of spikes occurring within the displayed window falls from about twenty to fewer than ten, while T_1 decreases from approximately 3.9 at $q = 0.96$ and 0.975 to 2.5 at $q = 0.98$ and 1.9 at $q = 0.99$. The two trends act in opposite directions: fewer spikes are produced, but a larger fraction of them qualify as extreme events, because the reduced variability of the local maxima lowers the threshold. At $q = 0.99$, essentially every spike in the record exceeds T_1. Extreme events are therefore present throughout the q range examined, consistent with the vertical extent of the green band in Fig. 13a, but their statistical character changes with q. At small fractional orders they are comparatively frequent events drawn from a broad distribution of spike amplitudes, whereas at larger q they are rare, isolated excursions from an almost silent background.

The multiplier in Eq. (23) is conventional rather than statistical; thresholds of the form $\mu_{x_i} + d\sigma_{x_i}$ with $4 \leq d \leq 8$ is standard in the extreme-event literature; the value used here follows [47,48]. The Gaussian 3σ and 6σ rules do not apply, since the local maxima are strongly non-Gaussian. The region of occurrence in Fig. 13a is unchanged for any $4 \leq d \leq 8$, whereas for $d \leq 3$, the threshold falls within the range of ordinary spike amplitudes and events are registered throughout the parameter plane, including where the dynamics are not extreme.

The events reported here are rare excursions exceeding the ongoing activity by more than an order of magnitude, and they occur only at the onset of desynchronization rather than within the asynchronous regime. Their phenomenology is that of paroxysmal large-amplitude population discharges, discussed previously in terms of extreme events in excitable systems [51]. Since the Chialvo map is a generic model with dimensionless variables, this correspondence is qualitative; what it indicates is that the transition in collective state, rather than the absence of synchrony itself, generates the rare large events.

4 Conclusions

A fractional-order version of the two-dimensional Chialvo neuron map was studied using the Caputo fractional difference operator. This formulation extends the classical discrete Chialvo model by incorporating memory effects, which are important for representing neuronal processes more realistically.

The stability analysis established that the model possesses a unique equilibrium for the parameter values considered, located at the center of the inner spiral of the phase portrait, and that its Jacobian has a complex-conjugate pair of eigenvalues. The equilibrium is asymptotically stable below a critical fractional order of approximately 0.951 and loses stability above it through a Neimark–Sacker bifurcation, giving rise to an invariant circle whose radius grows continuously from zero. This prediction was confirmed numerically, and in the integer-order limit the fixed point of the classical Chialvo map is recovered as unstable, consistent with its chaotic bursting. The fractional order therefore governs the stability of the resting state: strong memory stabilizes it, whereas weak memory destabilizes it and initiates a transition to oscillatory, and ultimately chaotic, firing.

A detailed bifurcation analysis, supported by LLE diagrams and two-dimensional regime maps, showed that the fractional order acts on the four model parameters in distinct ways. For three of them, the entire regime sequence—chaos, quasiperiodicity, fixed point—is displaced toward lower parameter values as the fractional order decreases, and the boundary separating the quasiperiodic and fixed-point regions coincides with the analytically obtained Neimark–Sacker curve. The effect is strongest for the bias parameter, for which chaotic firing disappears entirely at the smallest fractional order examined, and weakest for the offset. The remaining parameter behaves differently: the ordering of its regimes is reversed, its stability boundary migrates in the opposite direction, and the fractional order reshapes the arrangement of its chaotic and periodic regions rather than merely translating them. The LLE also increases monotonically with the

fractional order, so that memory controls not only the extent of the chaotic regions but the intensity of the chaos within them.

The collective behavior of 100 globally coupled maps was then examined under electrical, inner-linking, and chemical coupling. Complete synchronization was attained under all three schemes over considerable regions of the parameter space, with a lower onset under inner-linking than under electrical coupling. Since diffusive couplings vanish on the synchronization manifold, the synchronous state reproduces the dynamics of the isolated neuron, which explains why synchronizing a fixed point requires negligible coupling, whereas synchronizing chaotic motion requires substantially more. Below the synchronization threshold, both diffusive schemes organize the network into antiphase clusters and subsequently into solitary states; although no coexisting attractors were found for the isolated neuron, the coupled network supports several distinct dynamical states simultaneously. Chemical coupling behaves differently in every respect: its synchronization manifold departs from the isolated dynamics, it produces synchronized oscillation death, it is the only scheme yielding phase synchronization without complete synchronization, and its synchronous state follows a period-doubling route to chaos as the coupling strength grows.

Extreme events were found to occur only within a narrow band of chemical coupling strength coinciding with the onset of desynchronization, and to be essentially independent of the fractional order. Within that band, increasing the fractional order reduces the frequency of the spikes while lowering the qualifying threshold, so that a larger fraction of them qualify as extreme. The coupling strength is thus identified as the parameter controlling extreme events in the networked case.

Overall, introducing fractional-order memory into the Chialvo neuron map substantially enriches its dynamical repertoire and, once the units are coupled, produces a range of collective states—cluster and solitary states, oscillation death, phase synchronization, and extreme events—that the isolated model does not display. These properties make the model a useful computational framework for studying memory-dependent neuronal dynamics, collective behavior, and rare events.

Several limitations of the present study should be acknowledged. The network considered here is globally coupled and consists of 100 identical, noise-free units sharing a common fractional order. This configuration isolates the effect of the coupling function but, by construction, precludes the spatially organized states—chimeras, spiral waves, and traveling patterns—that require non-local or complex connectivity, and it does not address the heterogeneity of memory expected among biological neurons. The stability analysis of Section 3.1 is likewise local: it establishes the asymptotic stability of the equilibrium of the isolated map, but no analytical criterion for the stability of the synchronization manifold of the coupled fractional-order system is derived, so that the synchronization thresholds reported in Section 3.3 rest on numerical evidence alone. From a computational standpoint, the Caputo difference retains the entire history of the trajectory, so that the cost of evaluating the exact solution in Eq. (13) grows linearly with the iteration index, in contrast to the constant cost per step of the integer-order map; this burden is intrinsic to the formulation, since it is the retention of the full history that produces the memory effects under study, and it was the principal factor limiting the resolution of the parameter scans presented here. The truncated form of Eq. (14), employed at large n, is an approximation whose effect on the reported bifurcation structure has not been quantified here. Finally, extreme events have been identified through a single threshold criterion based on the mean and standard deviation of the local maxima, which establishes their existence and locates them in parameter space but stops short of a full statistical characterization of their amplitude distribution and recurrence times.

These limitations suggest several concrete directions for future work. The map-based fractional formulation is well suited to digital hardware realization, since the Caputo difference reduces to a weighted sum of past states that maps directly onto fixed-point FPGA or DSP arithmetic, while the short-memory principle bounds the required storage; an experimental implementation would allow the dynamics reported

here to be validated in real time and would open the model to neuromorphic and pseudorandom-sequence applications. The synchronization study can be scaled beyond the globally coupled case to non-locally coupled rings, small-world, scale-free, multiplex, and two-dimensional lattice topologies, in which the antiphase clusters and solitary states observed here may develop into chimera states and other spatiotemporal patterns. Introducing heterogeneity in the fractional order across the network, together with time-delayed and adaptive couplings that emulate synaptic plasticity, would bring the model closer to the diversity of real neuronal populations. On the analytical side, deriving a master-stability-function framework for coupled Caputo-type difference systems would place the numerically obtained synchronization thresholds on a rigorous footing. Lastly, a fuller statistical treatment of the extreme events—including fitting extreme-value distributions to the spike amplitudes, analyzing inter-event intervals, and assessing strategies for their prediction and suppression—would clarify their mechanisms and their possible relevance to pathological synchronization phenomena in the brain.

Acknowledgement: Not applicable.

Funding Statement: This work is based upon research funded by Iran National Science Foundation (INSF) under project No. 40502376 and is partially funded by SRM Group of Institutions vide funding number SRM/EEC/RI/CFR/005. M.P. was supported by the Slovenian Research and Innovation Agency (Javna agencija za znanstvenoraziskovalno in inovacijsko dejavnost Republike Slovenije) (Grant No. P1-0403).

Author Contributions: The authors confirm contribution to the paper as follows: Conceptualization: Sajad Jafari; Methodology: Karthikeyan Rajagopal; Software: Anitha Karthikeyan; Visualization: Anitha Karthikeyan and Mahtab Mehrabbeik; Investigation: Karthikeyan Rajagopal; Validation: Sajad Jafari and Matjaž Perc; Supervision: Matjaž Perc; Draft manuscript preparation: Anitha Karthikeyan and Mahtab Mehrabbeik; Manuscript review and editing: Karthikeyan Rajagopal, Sajad Jafari and Matjaž Perc; funding acquisition: Mahtab Mehrabbeik and Matjaž Perc. All authors reviewed and approved the final version of the manuscript.

Availability of Data and Materials: The data that support the findings of this study are available from the corresponding author, upon reasonable request.

Ethics Approval: Not applicable.

Conflicts of Interest: The authors declare no conflicts of interest.

References

1. Oliveri H, Goriely A. Mathematical models of neuronal growth. Biomech Model Mechanobiol. 2022;21(1):89–118.
2. Ma J, Zhao J, Wang B, Wang C. Physical approach to control ion channel in a neuron. Chaos Solitons Fractals. 2026;208:118079. doi:10.1016/j.chaos.2026.118079.
3. Wang B, Zhao J, Lei Z, Ma J. Controlling neural activity by shunting channel current in a memristive FitzHugh–Nagumo circuit. Chaos. 2026;36(5):053110.
4. Ibarz B, Casado JM, Sanjuán MA. Map-based models in neuronal dynamics. Phys Rep. 2011;501(1–2):1–74. doi:10.1016/j.physrep.2010.12.003.
5. Hodgkin AL, Huxley AF. A quantitative description of membrane current and its application to conduction and excitation in nerve. J Physiol. 1952;117(4):500.
6. Hindmarsh J, Rose R. A model of neuronal bursting using three coupled first order differential equations. Proc R Soc B Biol Sci. 1984;221(1222):87–102. doi:10.1098/rspb.1984.0024.
7. Rulkov NF. Modeling of spiking-bursting neural behavior using two-dimensional map. Phys Rev E. 2002;65(4):041922. doi:10.1103/physreve.65.041922.
8. Chialvo DR. Generic excitable dynamics on a two-dimensional map. Chaos Solitons Fractals. 1995;5(3):461–79.

9. Rothman JS, Silver RA. Data-driven modeling of synaptic transmission and integration. Prog Mol Biol Transl Sci. 2014;123(1):305–50. doi:10.1016/b978-0-12-397897-4.00004-8.
10. Claverol ET, Brown AD, Chad JE. Discrete simulation of large aggregates of neurons. Neurocomputing. 2002;47(1):277–97.
11. Li B, He Z. Bifurcations and chaos in a two-dimensional discrete Hindmarsh–Rose model. Nonlinear Dyn. 2014;76(1):697–715. doi:10.1007/s11071-013-1161-8.
12. Bao H, Hua Z, Liu W, Bao B. Discrete memristive neuron model and its interspike interval-encoded application in image encryption. Sci China Technol Sci. 2021;64(10):2281–91.
13. Zandi-Mehran N, Panahi S, Hosseini Z, Hashemi Golpayegani SMR, Jafari S. One dimensional map-based neuron model: a phase space interpretation. Chaos Solitons Fractals. 2020;132:109558.
14. Ramakrishnan B, Mehrabbeik M, Parastesh F, Rajagopal K, Jafari S. A new memristive neuron map model and its network's dynamics under electrochemical coupling. Electronics. 2022;11(1):153. doi:10.3390/electronics11010153.
15. Li K, Bao H, Li H, Ma J, Hua Z, Bao B. Memristive Rulkov neuron model with magnetic induction effects. IEEE Trans Industr Inform. 2022;18(3):1726–36. doi:10.1109/tii.2021.3086819.
16. Miller KS, Ross B. Fractional difference calculus. In: Proceedings of the International Symposium on Univalent Functions, Fractional Calculus and Their Applications; 1988 May 1–5; Koriyama, Japan. p. 139–52.
17. Diaz J, Osler T. Differences of fractional order. Math Comp. 1974;28(125):185–202.
18. Gray HL, Zhang NF. On a new definition of the fractional difference. Math Comp. 1988;50(182):513–29.
19. Holm M. The theory of discrete fractional calculus: development and application. Lincoln, NE, USA: The University of Nebraska-Lincoln; 2011.
20. Lu YM, Wang CH, Deng QL, Xu C. The dynamics of a memristor-based Rulkov neuron with fractional-order difference. Chin Phys B. 2022;31(6):060502.
21. Abdeljawad T. On Riemann and Caputo fractional differences. Comput Math Appl. 2011;62(3):1602–11.
22. Al-Nana A, Batiha IM. Modeling adaptive memory in neural dynamics: a dual nabla fractional-order FitzHugh–Nagumo framework. Ricerche Mat. 2026;75(3):1559–77.
23. Abbes A, Ouannas A, Shawagfeh N, Grassi G. The effect of the Caputo fractional difference operator on a new discrete COVID-19 model. Results Phys. 2022;39(1):105797. doi:10.1016/j.rinp.2022.105797.
24. Brandibur O, Kaslik E. Stability properties of a two-dimensional system involving one Caputo derivative and applications to the investigation of a fractional-order Morris–Lecar neuronal model. Nonlinear Dyn. 2017;90(4):2371–86. doi:10.1007/s11071-017-3809-2.
25. Dhakshinamoorthy V, Banerjee S. Fractional order mem-elements: from modeling to applications: a review. Nonlinear Dyn. 2026;114(7):503.
26. Atıcı FM, Şengül S. Modeling with fractional difference equations. J Math Anal Appl. 2010;369(1):1–9.
27. Khennaoui AA, Ouannas A, Boulaaras S, Pham VT, Taher Azar A. A fractional map with hidden attractors: chaos and control. Eur Phys J Spec Top. 2020;229(6):1083–93. doi:10.1140/epjst/e2020-900177-6.
28. Danca MF. Fractional order logistic map: numerical approach. Chaos Solitons Fractals. 2022;157:111851. doi:10.1016/j.chaos.2022.111851.
29. Rajagopal K, Nazarimehr F, Karthikeyan A, Alsaedi A, Hayat T, Pham VT. Dynamics of a neuron exposed to integer- and fractional-order discontinuous external magnetic flux. Front Inf Technol Electron Eng. 2019;20(4):584–90.
30. Debbouche N, Ouannas A, Momani S, Cafagna D, Pham VT. Fractional-order biological system: chaos, multistability and coexisting attractors. Eur Phys J Spec Top. 2022;231(5):1061–70.
31. Jun D, Guang-jun Z, Yong X, Hong Y, Jue W. Dynamic behavior analysis of fractional-order Hindmarsh–Rose neuronal model. Cogn Neurodyn. 2014;8(2):167–75. doi:10.1007/s11571-013-9273-x.
32. Herrmann R. Fractional calculus. London, UK: World Scientific; 2018.
33. Weinberg SH. Membrane capacitive memory alters spiking in neurons described by the fractional-order Hodgkin-Huxley model. PLoS One. 2015;10(5):e0126629. doi:10.1371/journal.pone.0126629.
34. Yu Y, Shi M, Kang H, Chen M, Bao B. Hidden dynamics in a fractional-order memristive Hindmarsh–Rose model. Nonlinear Dyn. 2020;100(1):891–906.

35. Chen S, Zou Y, Zhang X. An efficient method for Hopf bifurcation control in fractional-order neuron model. IEEE Access. 2019;7:77490–8. doi:10.1109/access.2019.2920007.
36. Alkhalaf S, Kumarasamy S, Arun S, Karthikeyan A, Boulaaras S. A fractional difference equation model of a simple neuron map. Fractals. 2022:2240263. doi:10.1142/S0218348X22402630.
37. Vivekanandhan G, Abdolmohammadi HR, Natiq H, Rajagopal K, Jafari S, Namazi H. Dynamic analysis of the discrete fractional-order Rulkov neuron map. Math Biosci Eng. 2023;20(3):4760–81. doi:10.1140/epjs/s11734-023-00912-7.
38. Teka WW, Upadhyay RK, Mondal A. Spiking and bursting patterns of fractional-order Izhikevich model. Commun Nonlinear Sci Numer Simul. 2018;56(36):161–76. doi:10.1016/j.cnsns.2017.07.026.
39. Ramadoss J, Alharbi A, Rajagopal K, Boulaaras S. A fractional-order discrete memristor neuron model: nodal and network dynamics. Electron Res Arch. 2022;30(11):3977–92.
40. Lin H, Wang C, Sun Y, Yao W. Firing multistability in a locally active memristive neuron model. Nonlinear Dyn. 2020;100(4):3667–83. doi:10.1007/s11071-020-05687-3.
41. Meucci R, Euzzor S, Ciofini M, Lapucci A, Zambrano S. Demonstrating filtered feedback control near a boundary crisis. IEEE Trans Circuits Syst I Regul Pap. 2021;68(7):3023–30.
42. Prakash P, Rajagopal K, Singh JP, Roy BK. Megastability, multistability in a periodically forced conservative and dissipative system with signum nonlinearity. Int J Bifurcat Chaos. 2018;28(9):1830030.
43. Xu Q, Liu T, Feng CT, Bao H, Wu HG, Bao BC. Continuous non-autonomous memristive Rulkov model with extreme multistability. Chin Phys B. 2021;30(12):128702.
44. Bao B, Hu J, Cai J, Zhang X, Bao H. Memristor-induced mode transitions and extreme multistability in a map-based neuron model. Nonlinear Dyn. 2023;111(4):3765–79. doi:10.21203/rs.3.rs-1715975/v1.
45. Mehrabbeik M, Jafari S, Meucci R, Ghosh D. Synchronization and multistability in a network of diffusively coupled laser models. Commun Nonlinear Sci Numer Simul. 2023;125:107380. doi:10.1016/j.cnsns.2023.107380.
46. Mehrabbeik M, Parastesh F, Rajagopal K, Jafari S, Perc M. Minimal universal laser network model: synchronization, extreme events, and multistability. Nonlinear Eng. 2024;13(1):20240044.
47. Nag Chowdhury S, Ray A, Dana SK, Ghosh D. Extreme events in dynamical systems and random walkers: a review. Phys Rep. 2022;966:1–52.
48. Nag Chowdhury S, Ray A, Mishra A, Ghosh D. Extreme events in globally coupled chaotic maps. J Phys Complex. 2021;2(3):035021. doi:10.1088/2632-072x/ac221f.
49. Mishra A, Saha S, Vigneshwaran M, Pal P, Kapitaniak T, Dana SK. Dragon-king-like extreme events in coupled bursting neurons. Phys Rev E. 2018;97(6):062311. doi:10.1103/physreve.97.062311.
50. Ray A, Rakshit S, Ghosh D, Dana SK. Intermittent large deviation of chaotic trajectory in Ikeda map: signature of extreme events. Chaos. 2019;29(4):043131.
51. Ansmann G, Karnatak R, Lehnertz K, Feudel U. Extreme events in excitable systems and mechanisms of their generation. Phys Rev E. 2013;88(5):052911. doi:10.1103/physreve.88.052911.
52. Arenas A, Díaz-Guilera A, Kurths J, Moreno Y, Zhou C. Synchronization in complex networks. Phys Rep. 2008;469(3):93–153. doi:10.1016/j.physrep.2008.09.002.
53. Fell J, Axmacher N. The role of phase synchronization in memory processes. Nat Rev Neurosci. 2011;12(2):105–18. doi:10.1038/nrn2979.
54. Rybalova E, Strelkova G, Schöll E, Anishchenko V. Relay and complete synchronization in heterogeneous multiplex networks of chaotic maps. Chaos. 2020;30(6):061104.
55. Andrzejak RG, Ruzzene G, Malvestio I, Schindler K, Schöll E, Zakharova A. Mean field phase synchronization between chimera states. Chaos. 2018;28(9):091101.
56. Parastesh F, Jafari S, Azarnoush H, Shahriari Z, Wang Z, Boccaletti S, et al. Chimeras. Phys Rep. 2021;898:1–114.
57. Wang S, Wei Z. Synchronization of coupled memristive Hindmarsh–Rose maps under different coupling conditions. AEU Int J Electron Commun. 2023;161(3):154561. doi:10.1016/j.aeue.2023.154561.
58. Fan W, Wu H, Li Z, Xu Q. Synchronization and chimera in a multiplex network of Hindmarsh–Rose neuron map with flux-controlled memristor. Eur Phys J Spec Top. 2022;231(22):4131–41. doi:10.1140/epjs/s11734-022-00720-5.

59. Fan W, Chen X, Wu H, Li Z, Xu Q. Firing patterns and synchronization of Morris-Lecar neuron model with memristive autapse. AEU Int J Electron Commun. 2023;158(5):154454. doi:10.1016/j.aeue.2022.154454.
60. Li T, Wang G, Yu D, Ding Q, Jia Y. Synchronization mode transitions induced by chaos in modified Morris–Lecar neural systems with weak coupling. Nonlinear Dyn. 2022;108(3):2611–25. doi:10.1007/s11071-022-07318-5.
61. Hussain I, Jafari S, Ghosh D, Perc M. Synchronization and chimeras in a network of photosensitive FitzHugh–Nagumo neurons. Nonlinear Dyn. 2021;104(3):2711–21. doi:10.1007/s11071-021-06427-x.
62. Yu D, Lu L, Wang G, Yang L, Jia Y. Synchronization mode transition induced by bounded noise in multiple time-delays coupled FitzHugh–Nagumo model. Chaos Solitons Fractals. 2021;147(4):111000. doi:10.1016/j.chaos.2021.111000.
63. Sun H, Cao H. Complete synchronization of coupled Rulkov neuron networks. Nonlinear Dyn. 2016;84(4):2423–34. doi:10.1007/s11071-016-2654-z.
64. Hu D, Cao H. Stability and synchronization of coupled Rulkov map-based neurons with chemical synapses. Commun Nonlinear Sci Numer Simul. 2016;35(2):105–22. doi:10.1016/j.cnsns.2015.10.025.
65. Rakshit S, Ray A, Bera BK, Ghosh D. Synchronization and firing patterns of coupled Rulkov neuronal map. Nonlinear Dyn. 2018;94(2):785–805. doi:10.1007/s11071-018-4394-8.
66. Lundstrom BN, Higgs MH, Spain WJ, Fairhall AL. Fractional differentiation by neocortical pyramidal neurons. Nat Neurosci. 2008;11(11):1335–42. doi:10.1038/nn.2212.
67. Čermák J, Győri I, Nechvátal L. On explicit stability conditions for a linear fractional difference system. Fract Calc Appl Anal. 2015;18(3):651–72. doi:10.1515/fca-2015-0040.